

# Angular momentum redistribution by SASI spiral modes and consequences for neutron star spins

Jérôme Guilet<sup>1,2</sup> and Rodrigo Fernández<sup>3,4,5</sup>

<sup>1</sup> *Department of Applied Mathematics and Theoretical Physics, University of Cambridge  
Centre for Mathematical Sciences, Wilberforce Road, Cambridge CB3 0WA, UK*

<sup>2</sup> *Max-Planck-Institut für Astrophysik, Karl-Schwarzschild-Str. 1, D-85748 Garching, Germany*

<sup>3</sup> *Institute for Advanced Study, Princeton, NJ 08540, USA*

<sup>4</sup> *Department of Physics, University of California, Berkeley, CA 94720, USA*

<sup>5</sup> *Department of Astronomy & Theoretical Astrophysics Center, University of California, Berkeley, CA 94720, USA*

4 October 2018

## ABSTRACT

In the collapsing core of massive stars, the standing accretion shock instability (SASI) can drive spiral modes that efficiently redistribute angular momentum. This process can impart a spin to the forming neutron star even when the progenitor star is non-rotating. Here we develop the first analytical description of the angular momentum redistribution driven by a spiral mode of the SASI. Our analysis, valid in the limit of small mode amplitude, shows that the angular momentum separation is driven by the Reynolds stress generated by the spiral mode. The resulting solutions compare favorably with previous three-dimensional hydrodynamic simulations of the SASI in the linear and weakly non-linear phases. Reasonable agreement is also found when extrapolating the solutions into the fully non-linear phase. A Reynolds-decomposition of the flow is performed in the saturated state of these simulations, showing that outward angular momentum transport by the Reynolds stress and the fluctuating component of the mass flux balance inward transport by advection. We derive an approximate analytic expression for the maximum angular momentum deposited in the neutron star as a function of the mass accretion rate, shock radius, shock compression ratio, and amplitude of the spiral mode at the time of explosion. Implications for the birth spin periods of neutron stars are discussed.

**Key words:** hydrodynamics – instabilities – shock waves – stars: neutron – stars: rotation – supernovae: general

## 1 INTRODUCTION

Neutron stars are formed during the gravitational collapse of massive stars. This core collapse also powers a supernova explosion that ejects the outer layers of the progenitor. The dynamics of the explosion has important consequences for the properties of the resulting neutron star, such as its final mass, space velocity, spin, and magnetic field (see, e.g., Janka 2012 for a review).

The most promising channel to drive an explosion for the majority of stellar progenitors is the so-called *neutrino mechanism*, in which neutrino energy deposition revives the stalled bounce accretion shock (Bethe & Wilson 1985). Breaking of the initial spherical symmetry is however key to a successful explosion (Liebendörfer et al. 2001; Rampp & Janka 2002; Thompson et al. 2003; Sumiyoshi et al. 2005). Asymmetries are caused primarily by two hydrodynamical instabilities that operate in the region between the neutrinosphere and

the shock: neutrino-driven convection (e.g., Herant et al. 1992), and the Standing Accretion Shock Instability (SASI; Blondin et al. 2003). Turbulence driven by these instabilities increases the efficiency of neutrino energy deposition by increasing the residency time of matter in the *gain* region, where heating dominates cooling, and by enlarging the postshock volume (e.g., Murphy & Burrows 2008; Marek & Janka 2009).

The SASI is a global oscillatory instability driven by an unstable cycle of advective and acoustic perturbations that propagate between the shock and a region of strong deceleration close to the proto-neutron star surface (Foglizzo et al. 2007; Foglizzo 2009; Guilet & Foglizzo 2012). For the conditions prevailing in core collapse supernovae, the instability is dominated by low-frequency, large-scale modes with spherical harmonic indices  $l \sim 1 - 2$  (Foglizzo et al. 2007; Yamasaki & Yamada 2007). In axisymmetric simulations, these modes manifest as sloshings of the shock along the

axis. Relaxing the constraint of axisymmetry allows the existence of spiral modes (Blondin & Mezzacappa 2007).

In the absence of initial rotation in the collapsing core, spiral SASI modes have the same linear growth rate as a sloshing mode with the same frequency and spherical harmonic index  $l$  (Foglizzo et al. 2007). A rotating progenitor favors the growth of prograde modes (Blondin & Mezzacappa 2007; Yamasaki & Foglizzo 2008; Iwakami et al. 2009). Hydrodynamic simulations without neutrino heating have shown that even in the absence of rotation, the non-linear evolution of SASI can lead to the dominance of a single spiral mode (Blondin & Mezzacappa 2007; Fernández 2010). This numerical result has been confirmed in an experimental analog of the SASI by Foglizzo et al. (2012). The timescale over which the spiral mode becomes dominant, and the conditions under which this happens are however not well understood. Furthermore, the interplay between the SASI and convection remains an open area of research (e.g., Scheck et al. 2008; Iwakami et al. 2008; Fernández & Thompson 2009a; Burrows et al. 2012; Müller et al. 2012; Murphy et al. 2013; Hanke et al. 2013; Iwakami et al. 2013; Fernández et al. 2014).

Blondin & Mezzacappa (2007) showed that SASI spiral modes have the ability to redistribute angular momentum in the postshock region, and suggested that this process could impart enough angular momentum to the neutron star to significantly change its spin. Blondin & Shaw (2007) and Fernández (2010) have more closely examined the process of angular momentum redistribution in spiral SASI flows, confirming the potential for neutron star spin-up. Foglizzo et al. (2012) later confirmed a redistribution of angular momentum by spiral modes in their experimental analog of SASI. All existing studies of this process are based on numerical simulations or experiments, however, and have not provided an analytical or physical description of this angular momentum separation.

It is the purpose of this paper to provide such an analytical description. In pursuing this, we set aside the broader question of the incidence of spiral modes in a realistic supernova context, particularly in relation to neutrino-driven convection. Such a topic is a current subject of debate in the literature (e.g., Janka et al. 2012; Burrows 2013), and progress on it requires work focused on the explosion dynamics. Here we confine ourselves to flows in which convection is weak relative to the SASI (e.g., as quantified by the ratio of advection time to convective growth time; Foglizzo et al. 2006; and as seen in the models of Müller et al. 2012), and which are such that the SASI grows to reach a quasi-steady state (e.g., prior to the onset of explosion). In addition to analytical studies, we carry out additional post-processing of the three-dimensional hydrodynamic simulations of Fernández (2010).

The paper is organised as follows. In Section 2, we derive a formalism which allows to compute the radial profile of angular momentum induced by a small amplitude spiral wave. These semi-analytical predictions are then successfully compared to the 3D simulations of Fernández (2010) in Section 3. The radial profiles of angular momentum driven by higher frequency harmonics display oscillations, which are explained in Appendix A using a decomposition of the perturbations into advected and acoustic waves. In Section 4, we analyse the non-linear phase of the SASI. Finally, in Sec-

tion 5 we derive an approximate analytical expression for the angular momentum contained in a spiral wave and therefore for the maximum angular momentum that can be imparted to the neutron star after the explosion has succeeded. The results are discussed and conclusions are drawn in Section 6.

## 2 FORMALISM

We consider a standing spherical accretion shock around a central proton-neutron star of mass  $M$  and radius  $r_*$  that is subject to a spiral SASI mode around some axis. The upstream accretion flow is non-rotating. The system is described using spherical polar coordinates  $\{r, \theta, \phi\}$  centred on the star. Following Fernández (2010), we define the surface integrated angular momentum density along the symmetry axis ( $z$ ) of the spiral mode as

$$l_z(r, t) \equiv \iint r \sin \theta \rho v_\phi \, d^2s = r^3 \iint \rho v_\phi \sin \theta \, d\Omega, \quad (1)$$

where  $\rho$  and  $v_\phi$  are the fluid density and azimuthal velocity, respectively. This expression is related to the total angular momentum  $L_z$  enclosed in a spherical shell between radii  $r_1$  and  $r_2$  by

$$L_z(r, t) = \int_{r_1}^{r_2} l_z \, dr. \quad (2)$$

Angular momentum conservation can then be written as

$$\partial_t l_z + \partial_r \mathcal{F} = 0, \quad (3)$$

where  $\mathcal{F}$  is the angular momentum flux integrated over a spherical surface

$$\mathcal{F}(r, t) \equiv r^3 \iint \rho v_r v_\phi \sin \theta \, d\Omega, \quad (4)$$

with  $v_r$  the radial velocity.

We assume that the flow can be described as a stationary background with superimposed small amplitude perturbations:

$$\rho(r, \theta, \phi, t) = \rho_0(r) + \delta\rho(r, \theta, \phi, t) + \delta^2\rho(r, \theta, \phi, t) + \dots \quad (5)$$

$$v_r = v_0 + \delta v_r + \delta^2 v_r + \dots \quad (6)$$

$$v_\phi = \delta v_\phi + \delta^2 v_\phi + \dots \quad (7)$$

where  $\delta$  and  $\delta^2$  denote first- and second order Eulerian perturbations, respectively, with  $\delta \gg \delta^2$ . We retain perturbations up to second order because this is the first non-zero contribution to the surface integrated angular momentum  $l_z$ . The evolution of the first order perturbations can be computed with a linear analysis as in Foglizzo et al. (2007).

In the following we assume that first-order perturbations can be decomposed into a superposition of modes with a spherical harmonic angular dependence with indices  $\{l, m\}$ , and the time-dependence of a plane wave with complex frequency  $\omega = \omega_r + i\omega_i$ , with  $\omega_r$  and  $\omega_i$  the real and imaginary parts, respectively. Except for transverse velocities, the space and time dependence of an arbitrary first-order perturbation  $\delta A$  is

$$\delta A(r, \theta, \phi, t) = \sum_{l, m} \text{Re} \left[ \delta \tilde{A}_{l, m}(r) e^{-i\omega t} Y_l^m(\theta, \phi) \right] \quad (8)$$

where  $\delta\tilde{A}_{l,m}(r)$  is the complex amplitude, and  $Y_l^m$  is a complex spherical harmonic. Transverse velocities have a different spatial dependence, and the azimuthal velocity satisfies

$$\delta v_\phi(r, \theta, \phi, t) = \sum_{l,m} \text{Re} \left[ \delta\tilde{v}_{\phi,l,m}(r) e^{-i\omega t} \frac{im}{\sin\theta} Y_l^m(\theta, \phi) \right]. \quad (9)$$

Note that the surface integral of all these first order perturbations vanishes (as long as  $l \neq 0$ ):

$$\iint \delta A(r, \theta, \phi, t) d^2s = 0. \quad (10)$$

The second order perturbations are so far unknown and their surface integral does not necessarily vanish.

Using the above decomposition, the surface integrated angular momentum density and flux can be expressed as

$$l_z = -\frac{\dot{M}r}{4\pi} \iint \left[ \frac{\delta\rho}{\rho_0} \frac{\delta v_\phi}{v_0} + \frac{\delta^2 v_\phi}{v_0} \right] \sin\theta d\Omega, \quad (11)$$

$$\mathcal{F} = l_z v_0 + T_{\text{Rey}} \quad (12)$$

where  $\dot{M} \equiv -4\pi r^2 \rho_0 v_0$  is the stationary mass flux, and  $T_{\text{Rey}}$  is the surface-integrated Reynolds stress associated with the SASI modes, defined by

$$T_{\text{Rey}}(r, t) \equiv \iint \rho_0 \delta v_r \delta v_\phi r \sin\theta d^2s. \quad (13)$$

$$= -\frac{\dot{M}r v_0}{4\pi} \iint \frac{\delta v_r \delta v_\phi}{v_0^2} \sin\theta d\Omega. \quad (14)$$

The stress can be computed using the linear eigenmodes

$$T_{\text{Rey}} = -\frac{\dot{M}r v_0}{4\pi} \iint \text{Re} \left( \sum_{l,m} \frac{\delta\tilde{v}_{\phi,l,m}}{v_0} e^{-i\omega_l t} \frac{im}{\sin\theta} Y_l^m \right) \times \text{Re} \left( \sum_{l',m'} \frac{\delta\tilde{v}_{r,l',m'}}{v_0} e^{-i\omega_{l'} t} Y_{l'}^{m'} \right) \sin\theta d\Omega \quad (15)$$

Using the relation  $\text{Re}(z_1)\text{Re}(z_2) = (z_1 + z_1^*)(z_2 + z_2^*)/4 = [\text{Re}(z_1 z_2^*) + \text{Re}(z_1 z_2)]/2$ , we obtain

$$T_{\text{Rey}} = -\frac{\dot{M}r v_0}{8\pi} \sum_{l,m} \sum_{l',m'} \text{Re} \left[ im \frac{\delta\tilde{v}_{\phi,l,m}}{v_0} \frac{\delta\tilde{v}_{r,l',m'}}{v_0} e^{-i(\omega_l + \omega_{l'})t} \iint Y_l^m Y_{l'}^{m'} d\Omega + im \frac{\delta\tilde{v}_{\phi,l,m}}{v_0} \frac{\delta\tilde{v}_{r,l',m'}^*}{v_0} e^{-i(\omega_l - \omega_{l'})t} \iint Y_l^m Y_{l'}^{m'*} d\Omega \right] \quad (16)$$

The first term inside the brackets vanishes for the following reasons. Since  $Y_l^{m*} = Y_l^{-m}$ , we have  $\iint Y_l^m Y_{l'}^{m'} d\Omega = 0$  unless  $\{l', m'\} = \{l, -m\}$ . This condition is met in two cases:  $m = m' = 0$  for which the term vanishes, or  $m = -m'$  for which the terms  $(m, -m)$  and  $(-m, m)$  cancel each other. Then the second term of equation (16) can be simplified using the relation  $\iint Y_l^m Y_{l'}^{m'*} d\Omega = \delta_{l,l'} \delta_{m,m'}$ , with  $\delta$  the Kronecker symbol. We then obtain

$$T_{\text{Rey}} = -\frac{\dot{M}r v_0}{8\pi} \sum_{l,m} \text{Re} \left[ im \frac{\delta\tilde{v}_{\phi,l,m}}{v_0} \frac{\delta\tilde{v}_{r,l,m}^*}{v_0} e^{2\omega_{l,t}} \right]. \quad (17)$$

Defining  $T_{\text{Rey}0,l,m}$  as the Reynolds stress amplitude of a

given mode with spherical harmonic indices  $\{l, m\}$  and with the time dependence scaled out,

$$T_{\text{Rey}0,l,m}(r) = -\frac{\dot{M}r v_0}{8\pi} \text{Re} \left[ im \frac{\delta\tilde{v}_{\phi,l,m}}{v_0} \frac{\delta\tilde{v}_{r,l,m}^*}{v_0} \right], \quad (18)$$

we can write equation (17) as

$$T_{\text{Rey}} = \sum_{l,m} T_{\text{Rey}0,l,m}(r) e^{2\omega_{l,t}}. \quad (19)$$

Combining equations (3), (12), and (19), we can write angular momentum conservation as a partial differential equation for the evolution of  $l_z$

$$\partial_t l_z + \partial_r(l_z v_0) = -\sum_{l,m} \partial_r T_{\text{Rey}0,l,m} e^{2\omega_{l,t}}. \quad (20)$$

The angular momentum density  $l_z$  can therefore be written as the sum of contributions from different spherical harmonics, with each term given by

$$\partial_t l_{z,l,m} + \partial_r(l_{z,l,m} v_0) = -\partial_r T_{\text{Rey}0,l,m} e^{2\omega_{l,t}}. \quad (21)$$

To solve equation (21), we look for a solution having the same time dependence as the Reynolds stress,

$$l_{z,l,m}(r, t) = l_{z0,l,m}(r) e^{2\omega_{l,t}}. \quad (22)$$

The partial differential equation is then reduced to an ordinary one:

$$\frac{d}{dr}(l_{z0,l,m} v_0) + \frac{2\omega_{l,l}}{v_0} l_{z0,l,m} v_0 = -\frac{d}{dr}(T_{\text{Rey}0,l,m}). \quad (23)$$

The spherically-integrated angular momentum density of a single mode is then

$$l_{z0,l,m} = -\frac{T_{\text{Rey}0,l,m}}{v_0} + \frac{e^{-2\omega_{l,l}\tau_{\text{adv}}}}{v_0} \int_{r_{\text{sh}}}^r \frac{2\omega_{l,l} e^{2\omega_{l,l}\tau_{\text{adv}}}}{v_0} T_{\text{Rey}0,l,m} dr, \quad (24)$$

where  $\tau_{\text{adv}}(r) = \int_{r_{\text{sh}}}^r dr/v_0$  is the advection time from the shock radius  $r_{\text{sh}}$  to a radius  $r < r_{\text{sh}}$ , and where we have used the following boundary condition at the shock:

$$\mathcal{F}(r_{\text{sh}}) = l_{z0}(r_{\text{sh}}) v_{\text{sh}} + T_{\text{Rey}0}(r_{\text{sh}}) = 0, \quad (25)$$

which follows from the vanishing angular momentum flux above the shock. The first term in Equation (24) describes a situation where the mode would not grow, while the second term, proportional to the growth rate, is a correction that takes into account the time dependence.

Note that a sum over spherical harmonics indices should be performed in order to obtain the total angular momentum density. Also note that while the angular momentum driven by spirals with different spherical harmonics indices simply adds up, the same is not true for several spiral modes with different frequencies but the same spherical harmonics indices. In the latter case, cross terms which are oscillatory in time would appear and would require a separate treatment which we do not provide here. A short discussion of the effect of higher frequency harmonics on the angular momentum redistribution is given in Section 3.3.

## 2.1 Angular momentum density below the shock

The angular momentum density below the shock due to a mode with spherical harmonic indices  $\{l, m\}$  follows from

equations (18) and (24),

$$l_{z\text{sh}} = -\frac{T_{\text{Re}y0}(r_{\text{sh}})}{v_{\text{sh}}} = \frac{\dot{M}r_{\text{sh}}}{8\pi} \text{Re} \left( \frac{im\delta\tilde{v}_\phi\delta\tilde{v}_r^*}{v_0^2} \right)_{\text{sh}} \quad (26)$$

This expression can be evaluated using the boundary conditions for the linear eigenmodes. The complex amplitude of the azimuthal velocity perturbation  $\delta\tilde{v}_\phi$  is (e.g. Guilet & Foglizzo 2012):

$$\left( \frac{\delta\tilde{v}_\phi}{v} \right)_{\text{sh}} = \frac{v_1 - v_{\text{sh}}}{v_{\text{sh}}} \frac{\Delta r}{r_{\text{sh}}}, \quad (27)$$

where  $v_1$  and  $v_{\text{sh}}$  are the radial velocities upstream and downstream of the shock, respectively. Given that this amplitude is real, only the imaginary part of the amplitude of the radial velocity perturbation matters for the angular momentum density:

$$\text{Im} \left( \frac{\delta\tilde{v}_r}{v} \right)_{\text{sh}} = -\frac{\omega_r r_{\text{sh}}}{v_{\text{sh}}} (1 - 1/\kappa) \frac{1 + 1/\mathcal{M}_1^2}{\gamma - (\gamma + 1)/\kappa + 1/\mathcal{M}_1^2} \frac{\Delta r}{r_{\text{sh}}}, \quad (28)$$

where  $\kappa \equiv v_1/v_{\text{sh}}$  is the compression ratio of the shock,  $\gamma$  is the adiabatic index of the gas, and  $\mathcal{M}_1$  is the upstream Mach number. Note that this equation is valid for a shock with a constant dissociation energy (e.g., Fernández & Thompson 2009b).

Combining Equations (26), (27) and (28), we can write

$$\frac{l_{z\text{sh}}}{\dot{M}r_{\text{sh}}} = -m \frac{\omega_r r_{\text{sh}}}{2\pi v_{\text{sh}}} f(\kappa, \mathcal{M}_1) \left( \frac{\Delta r}{r_{\text{sh}}} \right)^2, \quad (29)$$

where  $f(\kappa, \mathcal{M}_1)$  is a dimensionless factor,

$$f(\kappa, \mathcal{M}_1) \equiv \frac{1}{4} (\kappa - 1) (1 - 1/\kappa) \frac{1 + 1/\mathcal{M}_1^2}{\gamma - (\gamma + 1)/\kappa + 1/\mathcal{M}_1^2}. \quad (30)$$

For a strong ( $\mathcal{M}_1 \rightarrow \infty$ ) adiabatic shock this expression yields  $f = 1/(\gamma^2 - 1) = 1.29$  (with  $\gamma = 4/3$ ), while for an adiabatic shock with  $\mathcal{M}_1 = 5$  as studied in Section 3, we obtain  $f = 1.04$ . The dependence of the numerical factor  $f$  on the compression ratio  $\kappa$  and the upstream Mach number  $\mathcal{M}_1$  is shown in Figure 1 (the dissociation energy is varied when keeping one parameter constant). The dependence on  $\mathcal{M}_1$  for a fixed  $\kappa$  is very weak; it is even exactly independent of  $\mathcal{M}_1$  if  $\kappa = (\gamma + 1)/(\gamma - 1)$ , i.e., if the compression ratio is that of a strong adiabatic shock. Interestingly, the angular momentum density below the shock increases with  $\kappa$ , and the dependence is very close to linear, with  $f(\kappa, \mathcal{M}_1) \simeq 0.185\kappa$  providing a very good fit when  $\gamma = 4/3$ . A typical value of the compression ratio in the context of supernovae  $\kappa \sim 10$  yields  $f = 1.85$ , which is somewhat larger than for an adiabatic shock. Note also that the angular momentum density has the same sign as  $m$  since  $v_{\text{sh}}$  is a negative quantity.

### 3 ANGULAR MOMENTUM PROFILE IN THE LINEAR PHASE

Here we use the formalism of Section 2 to compute the angular momentum profile during the linear phase of the SASI, and compare the results with the 3D numerical simulations of Fernández (2010). The linear eigenmodes – computed numerically as in Guilet & Foglizzo (2012) – allow the construction of the Reynolds stress profile of each mode using

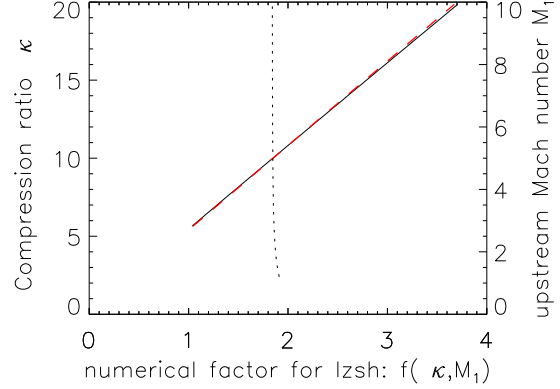


**Figure 1.** Dependence of the numerical factor  $f(\kappa, \mathcal{M}_1)$  that enters the angular momentum density (equation 29) on the shock compression ratio  $\kappa$  (left axis, full line) and on the upstream Mach number  $\mathcal{M}_1$  (right axis, dotted line). When varying one parameter we fixed the other one to  $\mathcal{M}_1 = 5$  and  $\kappa = 10$ , respectively (note that the shock dissociation energy must be varied for one of the parameters to remain constant). The red dashed line shows the fit  $f = 0.185\kappa$ .

equation (18). The contribution of a given mode to the angular momentum density profile is then obtained from equation (24). The amplitude of each of the spiral modes contributing to these profiles is extracted from the simulations as described in Appendix B. Two methods have been tried, which rely on a fit of the time-evolution of either the shock displacement or the transverse velocities at a given radius below the shock. In the rest of this section, the mode amplitude is extracted from the transverse velocities at a radius  $r = 0.8r_{s0}$  (Appendix B2), as it was found to give more accurate results.

The simulations of Fernández (2010) evolve the hydrodynamic equations with an initial condition equal to the stationary accretion shock system described in §2. The properties of the models studied are summarized in Table 3. Models are labeled by the ratio of the stellar to shock radius  $r_*/r_{s0}$ , which determines which modes become unstable when all other parameters are kept constant<sup>1</sup>. A given spiral mode is excited by placing an overdense shell with the same angular dependence in the upstream flow. We divide the rest of the discussion according to the type of mode in question: fundamental  $l = 1$  spiral mode (model R5\_L11\_HR), fundamental  $l = 2$  spiral mode (model R6\_L22\_P2), and a model with multiple unstable  $l = 1$  harmonics (R2\_L11h).

Unless otherwise noted, the system of units is based on the initial shock radius  $r_{s0}$ , free-fall velocity at the shock  $\sqrt{2GM/r_{s0}}$ , and upstream density  $\rho_1$ . For an easier connection with physical supernova parameters, however, we normalize the spherically-integrated Reynolds stress and angular momentum density by  $\dot{M}r_{\text{sh}0}|v_{\text{sh}0}|$  and  $\dot{M}r_{\text{sh}0}$ , respectively, where  $v_{\text{sh}0}$  is the downstream shock velocity.

<sup>1</sup> All models have upstream Mach number  $\mathcal{M}_1 = 5$ , adiabatic index  $\gamma = 4/3$ , vanishing energy flux upstream of the shock, and a cooling function  $\mathcal{L} \propto \rho P^{3/2}$ . The normalization of the latter is chosen so that the radial velocity vanishes at  $r = r_*$ .

**Table 1.** Summary of 3D models of Fernández (2010) with various derived quantities. Columns show model name, initial ratio of stellar to shock radius, indices of spiral mode excited  $\{l, m\}$ , ratio of mode frequency to advection frequency below the shock, amplitude of the mode in the saturated state, time interval for time average, and time-averaged angular momentum density from the simulation as well as from the analytic estimate in Section 5

Simulation name	$r_*/r_{s0}$	$\{l, m\}$	$\frac{\omega_r(r_{sh}-r_*)}{(2\pi v_{sh} )}$	Amplitude	time interval	$l_z/(\dot{M}r_{sh}^2)$ simulation	$l_z/(\dot{M}r_{sh}^2)$ analytic
R5_L11_HR	0.5	1,1	0.39	1.03	[75,125]	0.64	0.43
R6_L22_P2	0.6	2,2	0.44	0.36	[50,100]	0.21	0.12
R2_L11h	0.2	1,-1	0.42	1.31	[75,125]	-0.80	-0.76
R6_L21_P2	0.6	2,1	0.44	0.41	[50,100]	0.092	0.077
R2_L11f	0.2	1,1	0.42	1.16	[150,200]	0.74	0.59

### 3.1 Fundamental $l = 1$ spiral mode

Choosing  $r_*/r_{s0} = 0.5$  results in a configuration with an unstable fundamental  $l = 1$  mode with no unstable harmonics, and hence model R5\_L11\_HR is initially perturbed to excite the  $\{l, m\} = \{1, 1\}$  spiral. In order to compare directly the semi-analytical results with the simulations, we first extract the amplitude of the two  $m = \pm 1$  spiral modes using the method described in Appendix B2. The resulting amplitudes of the two spiral modes  $m = 1$  and  $m = -1$  at time  $t = 30$  are  $A_1 = 0.229$  and  $A_{-1} = 0.055$ , respectively. While the  $m = 1$  spiral is the dominant mode, the 20% contribution from the  $m = -1$  mode must be included to improve accuracy.

Figure 2 shows the projection of the radial velocity and azimuthal velocity times  $\sin\theta$  onto real spherical harmonics along the  $x$  and  $y$  axes. Profiles from the numerical simulation match those from linear theory with a very good accuracy showing that the method used to determine the amplitude of the spiral modes is accurate.

Figure 3 shows the radial profiles of the Reynolds stress and angular momentum integrated over a spherical surface (defined by Equations (14) and (1) respectively). The Reynolds stress is extracted from the simulation in two different ways. First, we subtract the advection of angular momentum by the mean flow ( $v_r l_z$  where  $l_z$  is the surface integrated angular momentum density and  $v_r$  is the angular average of the radial velocity) from the surface integrated total angular momentum flux defined by Equation (4) (the result is shown in black). Alternatively, we compute the Reynolds stress caused by the velocity perturbations projected on the  $\{l, m\} = \{1, 1\}$  spherical harmonic (red line). These two measures are in good agreement (except in the vicinity of the shock) showing that the Reynolds stress is indeed dominated by the  $\{l, m\} = \{1, 1\}$  SASI mode, and that the second order expansion is valid (otherwise higher order terms would appear, see Section 4.2).

The analytically predicted shapes of the Reynolds stress and angular momentum profiles agree very well with the numerical simulations. Radially inwards from the shock, the Reynolds stress first slightly increases, and then smoothly decreases to a very small value near the proto-neutron star surface. On the other hand, the angular momentum density changes sign at an intermediate radius: angular momentum redistribution caused by the Reynolds stress creates a region of positive angular momentum below the shock, and a region of negative angular momentum above the PNS surface.

Note that the amplitudes of the Reynolds stress and angular momentum density are higher in the numerical simulation by about 10–15%. The accuracy with which a code describes the linear coupling at the shock has been studied by Sato et al. (2009), who argued that the relevant parameter is the ratio  $\lambda_{adv}/\Delta r$ , where  $\lambda_{adv}$  is the wavelength of the advected wave created by the shock oscillation and  $\Delta r$  is the radial resolution. The radial resolution of the numerical simulation at the shock is  $\Delta r = 0.025r_{sh}$ . Using the frequency of the mode, we estimate  $\lambda_{adv}/\Delta r = 50$ . Comparing with Figure 10 of Sato et al. (2009), one may expect an accuracy of  $\sim 20\%$ , which is roughly consistent with the accuracy we obtain when comparing the simulations with the semi-analytical predictions.

### 3.2 Fundamental $l = 2$ spiral mode

With a larger proto-neutron star  $r_*/r_{sh} = 0.6$ , modes with  $l = 1$  are stable and  $l = 2$  has only its fundamental mode destabilized. Depending on the initial perturbations, both  $\{l, m\} = \{2, \pm 1\}$  or  $\{2, \pm 2\}$  may be excited preferentially. We here focus on model R6\_L22\_P2, which is initially perturbed so that an  $m = 2$  spiral mode dominates. Using the same method as for  $l = 1$ , we obtain the amplitudes of the two  $m = \pm 2$  spiral modes at time  $t = 30$ :  $A_2 = 0.185$  and  $A_{-2} = 0.021$ , respectively, showing that the  $m = 2$  mode is dominant and the  $m = -2$  mode contributes at the 10% level.

The Reynolds stress and angular momentum profile driven by this  $\{l, m\} = \{2, 2\}$  spiral mode are shown in Figure 4. Agreement between the numerical results and the analytical predictions is achieved within 30%, which is not as good as for  $l = 1$ . This is most likely due to the twice lower resolution used in this simulation. Interestingly, the shapes of both of these profiles are very similar to those of the spiral  $\{l, m\} = \{1, 1\}$  mode of model R5\_L11\_HR. Note however that the amplitudes of the Reynolds stress and of the angular momentum density for  $\{l, m\} = \{2, 2\}$  are larger by a factor of roughly two relative to that of the  $l = 1, m = 1$  mode, despite the fact that the mode amplitude is very similar. This factor is in fact predicted by equation (29), arising from the amplitude of the azimuthal velocity perturbation, which is proportional to the shock inclination in the azimuthal direction and therefore to the spherical harmonic index  $m$ .

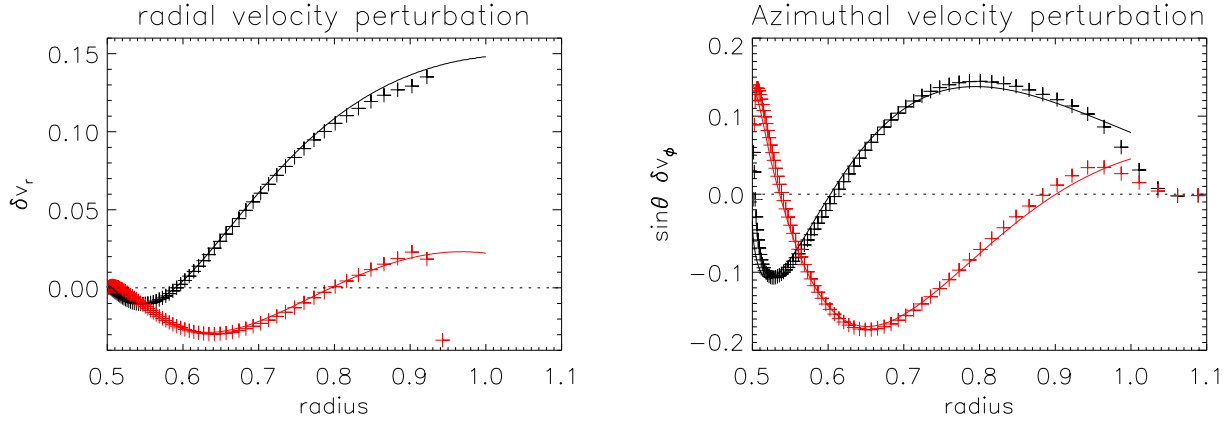


**Figure 2.** Radial profiles of radial velocity (left) and azimuthal velocity multiplied by  $\sin\theta$  (right), projected onto real  $l = 1$  spherical harmonics along the  $x$ -axis (black) and  $y$ -axis (red). The + signs show values from model R5\_L11\_HR at  $t = 30$ , while the full lines show the semi-analytical eigenmodes.

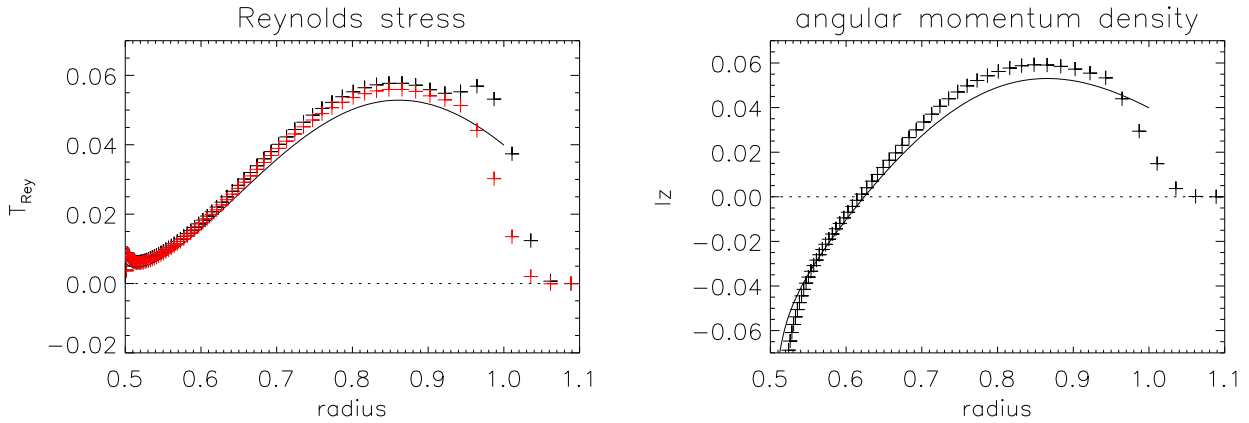


**Figure 3.** Radial profiles of the surface-integrated Reynolds stress (left) and angular momentum density (right) resulting from an  $l = 1$  spiral mode with  $r_*/r_{\text{sh}} = 0.5$ . The Reynolds stress is normalised by  $Mr_{\text{sh}0}|v_{\text{sh}0}|$ , while the angular momentum density is normalised by  $\dot{M}r_{\text{sh}0}$ . The + signs show values from model R5\_L11\_HR at  $t = 30$ , while the full lines show the semi-analytical predictions. The Reynolds stress is measured in the simulation in two different ways, as explained in the text (black and red colours).

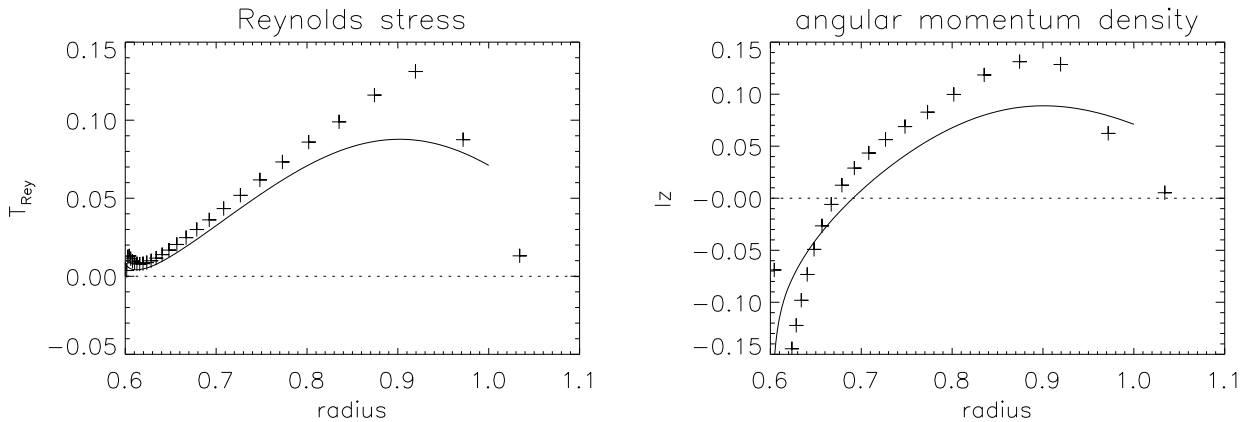


**Figure 4.** Radial profiles of the surface-integrated Reynolds stress (left) and angular momentum density (right) resulting from a  $\{l, m\} = \{2, 2\}$  spiral with  $r_*/r_{\text{sh}} = 0.6$ . The + signs show the result of model R6\_L22\_P2 at  $t = 30$ , while the full lines show the semi-analytical predictions.

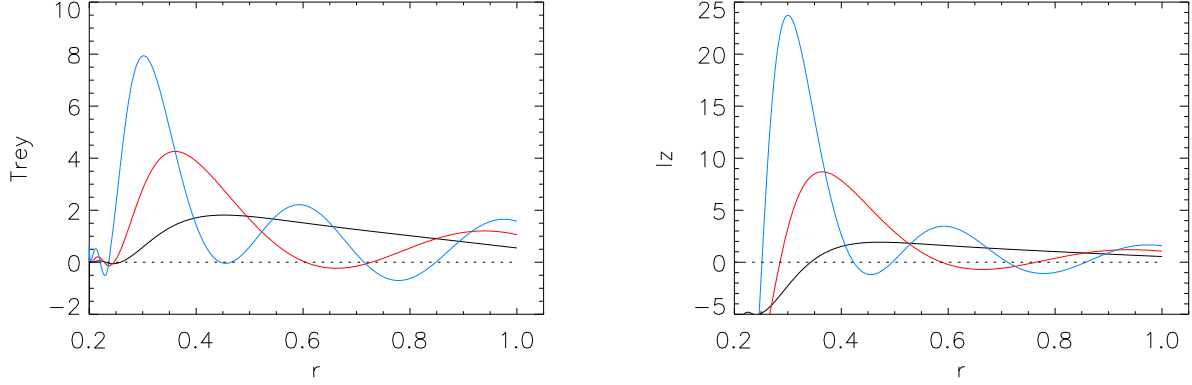


**Figure 5.** Analytical predictions for the surface-integrated Reynolds stress (left) and angular momentum density (right) associated with the first three  $l = 1$  harmonics ( $r_*/r_{\text{sh}} = 0.2$ ). The fundamental mode is shown in black, while the first and second harmonics are represented by red and blue lines, respectively.

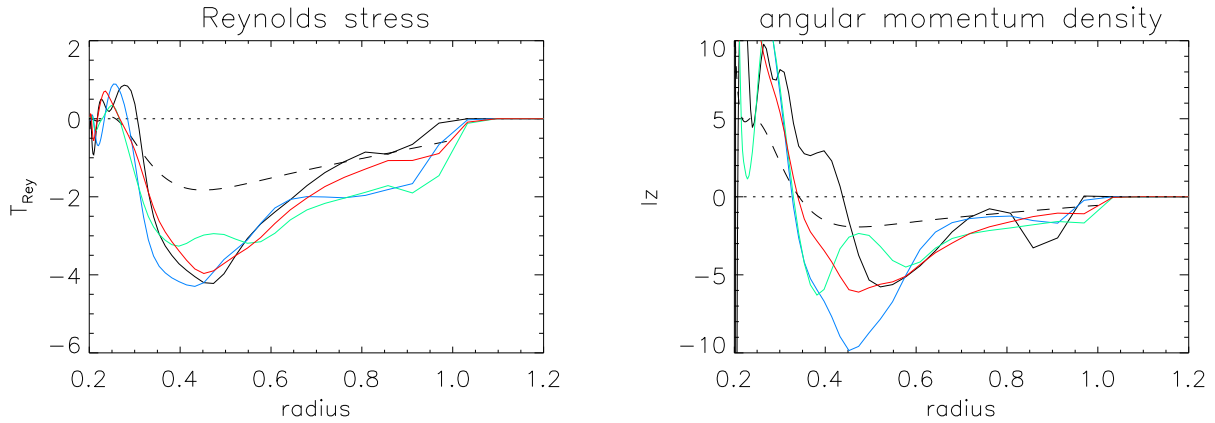


**Figure 6.** Surface-integrated Reynolds stress (left) and angular momentum density (right) in model R2\_L11h. The different colours represent different times:  $t = 25$  (black),  $t = 30$  (blue),  $t = 35$  (green) and  $t = 40$  (red). These profiles are renormalised by the quantity  $A_{-1}^2 - A_1^2$  (where  $A_1$  and  $A_{-1}$  are the amplitudes of the  $m = 1$  and  $m = -1$  spiral modes, obtained by fitting the shock deformation projected onto  $l = 1$  harmonics). The Reynolds stress has been computed using the first method described in Section 3.1. Furthermore, the semi-analytical prediction obtained with only the fundamental mode is shown with dashed lines.

### 3.3 Higher frequency harmonics of $l = 1$ spiral modes

For  $r_*/r_{\text{sh}} = 0.2$ , several harmonics of  $l = 1$  are unstable. The frequencies of the fundamental mode, as well as the first and second harmonics are  $\omega_r = \{0.53, 1.02, 1.52\}$ , and their growth rates are  $\omega_i = \{0.12, 0.10, 0.075\}$ , respectively. The fundamental mode has the largest growth rate and should therefore play a dominant role, which is consistent with the simulations. However, the growth rate of the two higher frequency harmonics is only slightly smaller (specially for the first harmonic), suggesting that they could also have an impact on the dynamics and angular momentum redistribution. The individual contributions of these three modes to the surface-integrated Reynolds stress and angular momentum density are illustrated in Figure 5. As predicted by Equation (29), the angular momentum density at the shock of a given mode is proportional to its frequency and therefore increases with increasing harmonic order.

The Reynolds stress and angular momentum density profiles generated by the fundamental mode are very similar to those obtained for different values of  $r_*/r_{\text{sh}}$ . In contrast, the profiles driven by the second and third harmonics have a more complex structure exhibiting radial oscillations. The profiles exhibit one more oscillation per increasing harmonic order.

These oscillations can be understood by decomposing the velocity perturbations below the shock into waves as described in Appendix A. The Reynolds stress is decomposed into six parts: three coming from the individual contributions of the vorticity wave and of the two acoustic waves propagating up and down, and three additional contributions arising from the interaction between these waves. It is shown in Appendix A that three of these contributions dominate: the individual contributions from the vorticity wave and the acoustic wave propagating upwards both create a *non-oscillatory* Reynolds stress profile with the same sign as  $m$ , while the interaction between these two waves

drives a Reynolds stress that *oscillates* in the radial direction between positive and negative values. The three other contributions play only a very minor role. The analysis of Appendix A shows that the oscillatory contribution is more important in the higher frequency harmonics than in the fundamental mode. Furthermore, if there is no phase shift in the wave coupling at the shock and in the deceleration region close to the neutron star surface, then the analysis predicts one oscillation in the fundamental mode Reynolds stress profile, two for the first harmonic, and three for the second harmonic. This is indeed the case in Figure 5, although the last half oscillation is difficult to see because it lies very close the PNS surface.

If there is a superposition of several  $l = 1$  unstable modes with different frequencies, the resulting Reynolds stress is not merely a superposition of the individual contributions from these modes. Instead, the interaction between the different modes generates additional components that oscillate in time. One would therefore expect the shape of the Reynolds stress profile to evolve in time and to display radial oscillations.

Figure 6 shows the surface-integrated Reynolds stress and angular momentum density in model R2\_L11h at times  $t = 25, 30, 35, 40$ . These profiles are renormalised by dividing by the quantity  $A_{-1}^2 - A_1^2$  (where  $A_1$  and  $A_{-1}$  are the amplitudes of the  $m = 1$  and  $m = -1$  spiral modes obtained by fitting the shock deformation projected onto  $l = 1$  harmonics). This renormalisation is chosen so that the analytical prediction is the same if only the fundamental mode were present. While the overall time evolution of the amplitude has been properly scaled out, the Reynolds stress and angular momentum density profiles still show radial oscillations which are time dependent. These oscillations might be attributed to the presence of smaller amplitude higher frequency harmonic modes in addition to the dominant fundamental.

Note that contrary to Section 3.1, the Reynolds stress deduced from the simulation with the two different methods differ at small radii. This indicates that higher  $l$  motions also play a role in determining the total Reynolds stress in this region.

## 4 NONLINEAR PHASE

All of the previous considerations are strictly valid only in the linear- or weakly-nonlinear phase of the SASI. Several effects neglected in our analytical treatment may appear in the fully non-linear phase: breakdown of mode linearity (saturation and higher-order terms), modification of ‘background’ quantities, and turbulent motions triggered by the SASI itself. Here we discuss the first and third effects in turn.

### 4.1 Quasi-Steady-State Solution

In the non-linear phase, the amplitude of the SASI spiral mode stops growing due in part to secondary instabilities (e.g., Guilet et al. 2010). We can approximately take this into account by assuming that the structure of the mode remains close to that given by the linear analysis, but then setting the growth rate to zero. In this case, the evolution

equation for the angular momentum (eq. 21) becomes:

$$\partial_t l_z + \partial_r(l_z v_0) = -\partial_r T_{Rey}, \quad (31)$$

where  $T_{Rey}$  is the Reynolds stress of the dominant spiral mode, which is now steady since the mode is not growing. This equation then admits the following stationary solution for the angular momentum profile:

$$l_z = -\frac{T_{Rey}}{v_0}. \quad (32)$$

This is the same as Equation (24) except for the absence of the second term due to the growth of the mode. As a consequence, the predicted angular momentum density has the same sign as the Reynolds stress, and therefore there is no sign change at an intermediate radius. This means that the matter with an angular momentum of opposite sign has been accreted onto the proto-neutron and either accumulated in the very dense region at the inner edge of the grid in the simulations, or left the numerical domain.

In Figure 7, the solution to equation 32 is compared with time-averaged profiles from models R6\_L22\_P2 (dominated by an  $\{l, m\} = \{2, 2\}$  spiral mode) and R6\_L21\_P2 (dominated by an  $\{l, m\} = \{2, 1\}$  mode). The time average is performed over the time interval  $t = [50, 100]$ , during which the spiral modes have an approximately constant amplitude. This amplitude can be measured by performing a fit like in Section 3, because the time evolution of the shock deformation is close to a sinusoid. The resulting amplitude is then used to normalize the analytic prediction.

Although the assumptions made in the analytical treatment are not well justified in the non-linear phase, Figure 7 shows that the analytical predictions are in fairly good agreement with the time-averaged profiles of angular momentum density. In particular, the angular momentum density profile does not change sign except very close to  $r_*$ , in contrast to the linear phase, being much better predicted by Equation (32) (full line) than by Equation (24) (dotted line). This rather good agreement is helped by the fact that the saturation amplitude is fairly low (compared to the simulation with  $l = 1$  SASI activity), and therefore the shock does not significantly expand due to the spiral mode activity.

Figure 8 shows results from the non-linear phase of model R5\_L11\_HR, which is dominated by a large amplitude  $\{l, m\} = \{1, 1\}$  spiral mode. In this model as well, the time-averaged angular momentum density profile does not change sign except very close to the PNS surface. In order to illustrate the time-evolution towards this new shape of the surface-integrated angular momentum density, we plot the instantaneous profiles at three different times:  $t = 50$ , just before the amplitude of the SASI mode saturates, and two later times ( $t = 65$  and  $t = 75$ ) that are well into the non-linear saturated phase. There is a large variation in the shape of the radial profile, most notably the radius where the angular momentum changes sign moves inward.

In order to compare the time-averaged profiles with the semi-analytical results, we estimate the amplitude of the



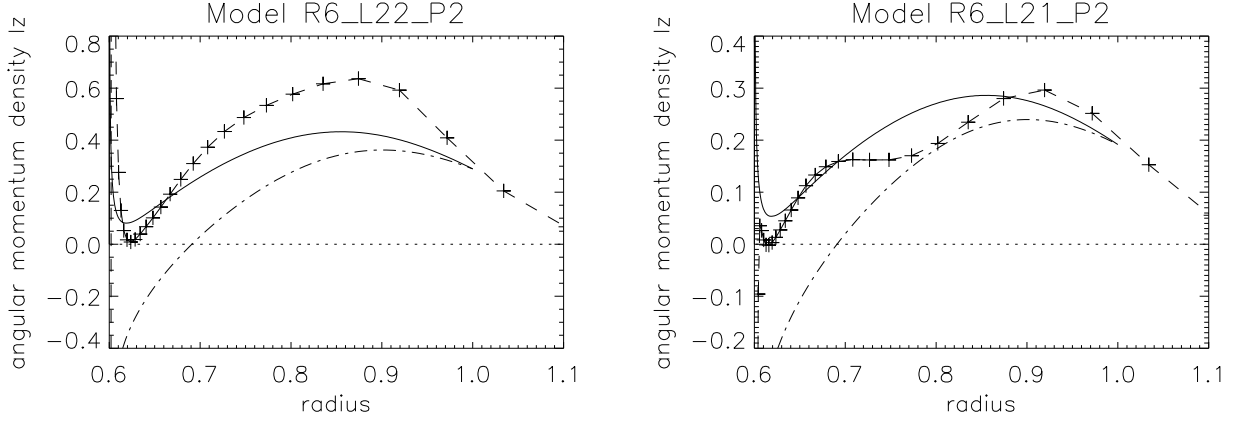


**Figure 7.** Time-averaged profiles of surface integrated angular momentum density in the non-linear phase of models R6.L22.P2 ( $\{l, m\} = \{2, 2\}$ , left panel) and R6.L21.P2 ( $\{l, m\} = \{2, 1\}$ , right panel). Simulation results are shown with + signs and a dashed line, while the analytical predictions extrapolated to the saturated phase are shown with full black lines (from eq. 32). For comparison, we also show the predicted angular momentum density in the case of a growing mode (from eq. 24, dot-dashed black line).

spiral mode in the saturated state as <sup>2</sup>

$$A_1 = \sqrt{2} \left( \overline{a_x^2 + a_y^2} \right)^{1/2}, \quad (33)$$

where  $a_x$  and  $a_y$  are the shock deformation amplitude projected onto real spherical harmonics along the  $x$  and  $y$  axis, the bar represents a time average, and the factor  $\sqrt{2}$  accounts for the different normalisation of real and complex spherical harmonics. For model R5.L11.HR we obtain an amplitude of  $A_1 = 1.03$ . Due to this large amplitude spiral mode, the shock significantly expands compared to its initial position, reaching an average radius of  $\simeq 1.4r_{\text{sh}0}$ . As a result, the time-averaged profiles of angular momentum density differ from the analytical predictions in that it extends to larger radii. It is also flatter than the analytical prediction, with a value close to the analytical value predicted at the shock.

## 4.2 Reynolds decomposition

To gain further insight into the angular momentum redistribution in the non-linear phase, we perform a Reynolds decomposition on the models of Table 3 and make use of conservation laws. Hereafter, the symbol  $\langle A \rangle$  is used to denote the time- and angle-average of a quantity  $A$ ,

$$\langle A \rangle(r) \equiv \frac{1}{4\pi(t_f - t_i)} \int_{t_i}^{t_f} dt \int_{4\pi} d\Omega A(r, \theta, \phi, t), \quad (34)$$

where  $t_i$  and  $t_f$  are the initial and final times chosen for the averaging interval.

<sup>2</sup> We did not measure the spiral mode amplitude with the method of Appendix B because the time evolution of the shock deformation projected onto spherical harmonics is irregular, yielding a poor-quality fit. We note that this alternative method to measure the spiral mode amplitude is accurate if a single spiral mode dominates the dynamics. For models R6.L22.P2 and R6.L21.P2, where a fit could be performed showing a dominant single spiral, the alternative method gives the same results as the fit.

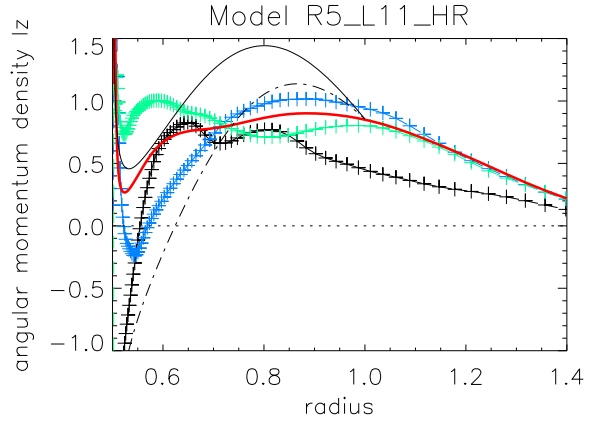


**Figure 8.** Surface-integrated angular momentum density in the non-linear phase of model R5.L11.HR. The + signs with dashed lines show instantaneous profiles at times  $t = 50$  (beginning of the saturated phase, black line),  $t = 65$  (blue line), and  $t = 75$  (green line). The red full line shows the time-averaged profile in the time interval  $t = [75, 125]$ , and the black full line shows the analytical prediction extrapolated to the saturated phase (using eq. [32]). For comparison, we also show with a dot-dashed black line the predicted angular momentum density in the case of a growing mode computed using Equation (24).

In a saturated state that is stationary in a time averaged sense, conservation of angular momentum (equation 3) becomes

$$\partial_r \langle \mathcal{F} \rangle = 4\pi \partial_r \langle r^2 \rho v_r (r \sin \theta v_\phi) \rangle = 0. \quad (35)$$

In the absence of rotation, we have  $\langle \mathcal{F} \rangle = 0$  upstream of the shock, therefore  $\langle \mathcal{F} \rangle = 0$  should be verified everywhere in the flow. Similarly, the equation of time-averaged mass conservation reads

$$\partial_r \langle r^2 \rho v_r \rangle = 0. \quad (36)$$

The mass accretion rate above the shock then sets the value of the mass flux everywhere,  $\langle r^2 \rho v_r \rangle = -\dot{M}/4\pi$ .

Now let us decompose the density, radial velocity, and

specific angular momentum

$$\lambda \equiv r \sin \theta v_\phi \quad (37)$$

into a mean value plus a fluctuating component with vanishing average,

$$\rho = \langle \rho \rangle + \Delta \rho, \quad (38)$$

$$v_r = \langle v_r \rangle + \Delta v_r, \quad (39)$$

$$\lambda = \langle \lambda \rangle + \Delta \lambda, \quad (40)$$

Note that contrary to previous sections, the fluctuating component is not assumed to be small. We will focus the discussion on the time-averaged, surface-integrated angular momentum flux,

$$\langle \mathcal{F} \rangle = 4\pi r^2 \langle \rho v_r \lambda \rangle. \quad (41)$$

Separating the radial velocity and specific angular momentum into mean and fluctuating components, we obtain

$$\langle \mathcal{F} \rangle = 4\pi r^2 [\langle \rho \lambda \rangle \langle v_r \rangle + \langle \rho \Delta v_r \Delta \lambda \rangle + \langle \Delta \rho \Delta v_r \rangle \langle \lambda \rangle]. \quad (42)$$

We recognise the first term on the right hand side as the angular momentum density advected by the mean flow, the second term as the mean Reynolds stress

$$\langle T_{Rey} \rangle \equiv 4\pi r^2 \langle \rho \Delta v_r \Delta \lambda \rangle, \quad (43)$$

and the third term as the angular momentum transported by the fluctuating component of the mass flux (see, e.g., Murphy & Meakin 2011 for the physical meaning of terms in the Reynolds-averaged fluid equations).

From equation (42) we can solve for the mean angular momentum density

$$\langle l_z \rangle = -\frac{\langle T_{Rey} \rangle}{\langle v_r \rangle} - \frac{4\pi r^2 \langle \lambda \rangle}{\langle v_r \rangle} \langle \Delta \rho \Delta v_r \rangle + \frac{\langle \mathcal{F} \rangle}{\langle v_r \rangle}. \quad (44)$$

The first term of on the r.h.s. mirrors the corresponding term in equations (24) and (32). The second term is not present in equation (24) because it is of higher order in the expansion of small mode amplitude.

Figure 9 shows the different terms that make up equation (44) applied to model R5\_L11\_HR, with the time-average taken over the interval  $[75, 125]t_{ff0}$ . The angular momentum flux  $\langle \mathcal{F} \rangle$  is smaller than the other terms by 2 orders of magnitude over most of the domain, verifying that global angular momentum conservation is satisfied to a reasonable degree. Very close to the neutron star surface, matter piles up and the system is never in steady-state, hence the non-zero  $\langle \mathcal{F} \rangle$  in that region.

The dominant contribution to the angular momentum density arises from the Reynolds stress, justifying equation (32) a posteriori. Near the shock, the component due to the fluctuating mass flux becomes important, though it never exceeds that due to the Reynolds stress. Note that in order to maintain steady-state, both terms must transport angular momentum outward to counteract advection by the mean flow.

The Reynolds stress has contributions from the large-scale saturated spiral mode as well as from smaller scale turbulent fluctuations. Further analysis in the space-time frequency domain could separate these components; we leave this for future work.

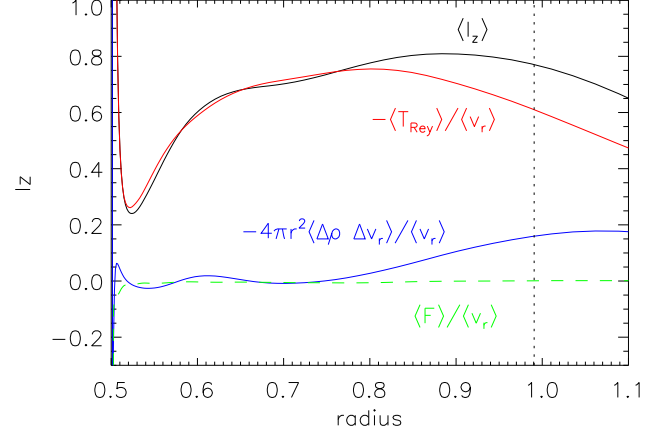


**Figure 9.** Time-averaged and surface-integrated angular momentum density as a function of radius (equation 44) for model R5\_L11\_HR (black). Also shown are the contributions from the mean Reynolds stress (red), the fluctuating component of the mass flux (blue), and the total angular momentum flux (green). The vertical dashed line marks the innermost radius affected by shock oscillations, defined as the average minimum shock radius minus one standard deviation (Fernández & Thompson 2009b).

## 5 APPROXIMATE EXPRESSION FOR THE MAXIMUM ANGULAR MOMENTUM CONTAINED IN A SPIRAL WAVE

A SASI spiral mode separates the postshock flow into a region below the shock where matter rotates in the same direction as the spiral mode, and another region further below where angular momentum has the opposite sign. The magnitude of this redistribution is

$$L_z = \int_{r_0}^{r_{sh}} l_z dr, \quad (45)$$

where  $r_0$  is the radius where the angular momentum density changes sign. We found in Section 4 that during the saturated phase, the angular momentum density profile in the SASI active region does not change sign except very close to the protoneutron star, indicating that matter with the opposite sign of angular momentum has been already accreted. We will therefore approximate the radius  $r_0$  by the radius of the proto-neutron star  $r_*$ . Figure 9 suggests that the angular momentum density has a rather flat profile; we will thus assume that the angular momentum density equals its value below the shock everywhere in the postshock region. Note that this assumption is only approximate and is based on an empirical observation rather than a strong theoretical argument. It would therefore be useful to check its validity in numerical simulations of less idealised flows, in particular including neutrino heating. The results of Section 3.3 and Appendix A show that the fundamental mode creates an angular momentum profile with much less radial structure than higher frequency harmonics. This suggests that our assumption might remain approximately valid as long as the dynamics is dominated by the fundamental mode.

Using these two simplifying assumptions, we can write the angular momentum magnitude as

$$L_z \simeq (r_{sh} - r_0) l_{zsh} \simeq (r_{sh} - r_*) l_{zsh}. \quad (46)$$

This equation can then be combined with equation (29) to

obtain an analytical estimate of the total angular momentum redistributed by a SASI spiral mode

$$L_z \simeq mf(\kappa, \mathcal{M}_1) \frac{\omega_r(r_{\text{sh}} - r_*)}{2\pi|v_{\text{sh}}|} \dot{M} r_{\text{sh}}^2 \left( \frac{\Delta r}{r_{\text{sh}}} \right)^2. \quad (47)$$

Note that equation (29) is still valid in the presence of neutrino heating, which (just like neutrino cooling) affects the angular momentum density below the shock only indirectly through its effect on the frequency of the mode and its saturation amplitude. For the fundamental mode, the frequency is approximately  $\omega_r \sim 2\pi/\tau_{\text{aac}}$ , where  $\tau_{\text{aac}}$  is the advective acoustic time (Foglizzo et al. 2007; Guilet & Foglizzo 2012), thus

$$\frac{\omega_r(r_{\text{sh}} - r_*)}{2\pi|v_{\text{sh}}|} \simeq \frac{\tau_{\text{aac}}(r_{\text{sh}} - r_*)}{|v_{\text{sh}}|}. \quad (48)$$

This ratio is expected to be  $\lesssim 1$ , because the advective-acoustic time  $\tau_{\text{aac}}$  is slightly longer than the advection time from the shock to the neutron star  $\tau_{\text{adv}}$ , and the advection time in turn is longer than that estimated with a constant velocity,  $(r_{\text{sh}} - r_*)/|v_{\text{sh}}|$ , because the flow is decelerated. The flows studied in Section 3 with different values of  $r_*/r_{\text{sh}}$  all satisfy  $\omega_r(r_{\text{sh}} - r_*)/(2\pi|v_{\text{sh}}|) \simeq 0.4$  (see Table 3).

In Table 3, we compare the angular momentum redistributed by a SASI spiral mode predicted by Equation (47) with the results of the numerical simulations of Fernández (2010). For this purpose the spiral mode amplitude is measured in the simulations following equation (33), the spiral mode frequency is taken to be that predicted by the linear analysis, and the shock radius that of the initial stationary state. For most simulations, the analytical prediction differs from the numerical result by a few tens of percents which is comparable to the accuracy found in the previous sections (the largest difference is for simulation R6\_L22\_P2 at 45%). Note that the analytical prediction tends to slightly underestimate the angular momentum measured in the numerical simulations; this might be due partly to the fact that the mean shock radius has expanded, allowing more angular momentum to accumulate.

We now turn to discuss the significance of these results for the spin of neutron stars at birth. The saturated SASI phase should end at the onset of explosion. The magnitude of the angular momentum imparted to the neutron star will depend on the radius separating expelled and accreted matter: if it is too deep in the postshock region in the case of an early explosion, matter with both signs of angular momentum will be ejected, reducing the total angular momentum (Rantsiou et al. 2011). Also, the magnitude of the angular momentum is also reduced if SASI activity occurs episodically as observed by Hanke et al. (2013) and Iwakami et al. (2013), in which case angular momentum with alternating signs is accreted onto the proto-neutron star. Nevertheless, we can estimate the maximum imparted angular momentum in the idealised scenario outlined by Blondin & Mezzacappa (2007), where all the matter rotating in the same direction as the SASI spiral mode is ejected.

Evaluating Equation (47), we obtain

$$L_z \simeq 2.3 \times 10^{46} \left( \frac{\kappa}{10} \right) \left( \frac{50 \text{ ms}}{P_{\text{sasi}}} \right) \left( \frac{r_{\text{sh}} - r_*}{120 \text{ km}} \right) \left( \frac{3000 \text{ km.s}^{-1}}{v_{\text{sh}}} \right) \times \left( \frac{\dot{M}}{0.3 M_{\odot} \text{.s}^{-1}} \right) \left( \frac{r_{\text{sh}}}{150 \text{ km}} \right)^2 \left( 3 \frac{\Delta r}{r_{\text{sh}}} \right)^2 \text{ g.cm}^2 \text{.s}^{-1}. \quad (49)$$

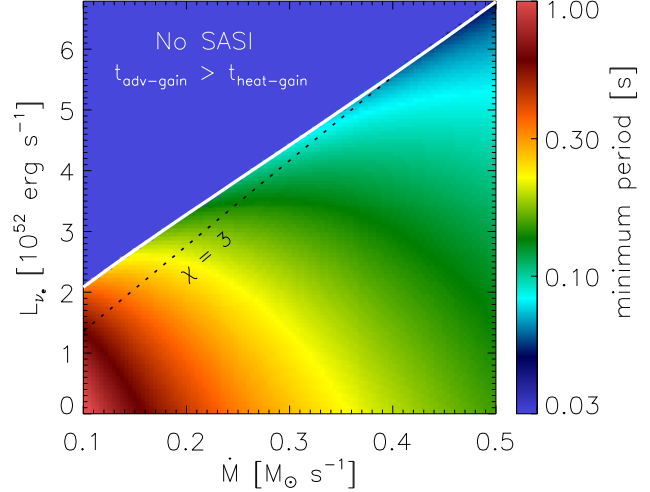


**Figure 10.** Minimum neutron star rotation period that can be generated via a spiral SASI mode, as inferred from equation (50). The input parameters (shock radius, shock compression ratio, SASI period, and postshock velocity) are computed from the steady-state solutions of Fernández (2012), which employ a realistic equation of state. The stellar radius is set to  $r_* = 30$  km, and the steady-state shock radius has been multiplied by a factor  $(1 + \Delta r/r_{s0})$ , with  $\Delta r/r_{s0} = 0.3$  a typical saturation value of the SASI. The region marked ‘No SASI’ is such that the runaway condition in spherical symmetry (Janka & Keil 1998; Thompson 2000; Thompson et al. 2005) is met, thus the SASI does not have time to develop before explosion. The dashed line shows the threshold  $\chi = 3$ , below which the SASI is expected to dominate the dynamics (Foglizzo et al. 2006).

Assuming a moment of inertia of the neutron star of  $I = I_{45} \times 10^{45} \text{ g.cm}^2$ , this can be translated into a minimum period of uniform rotation

$$P \simeq 290 I_{45} \left( \frac{10}{\kappa} \right) \left( \frac{P_{\text{sasi}}}{50 \text{ ms}} \right) \left( \frac{120 \text{ km}}{r_{\text{sh}} - r_*} \right) \left( \frac{v_{\text{sh}}}{3000 \text{ km.s}^{-1}} \right) \left( \frac{0.3 M_{\odot} \text{.s}^{-1}}{\dot{M}} \right) \left( \frac{150 \text{ km}}{r_{\text{sh}}} \right)^2 \left( \frac{r_{\text{sh}}}{3\Delta r} \right)^2 \text{ ms}. \quad (50)$$

Note the dependence on the square of the amplitude and the shock radius.

We have so far applied our analytical results to an idealised setup where only SASI develops due to the absence of heating. Our analytical treatment can in principle be applied more generally as long as a SASI spiral mode dominates the dynamics, and a comparison with more realistic simulations would be desirable. Figure 10 shows the result of evaluating equation (50) with parameters from the steady-state accretion shock models of Fernández (2012). These solutions employ the equation of state of Shen et al. (1998) as implemented by O’Connor & Ott (2010), and use a ‘lightbulb’ approximation to neutrino heating. The minimum period is computed as a function of the mass accretion rate and electron neutrino luminosity, taking<sup>3</sup>  $r_* = 30$  km. To account for the fact that in the saturated SASI phase the average shock radius is larger than the initial steady-state value,

<sup>3</sup> Other parameters are the same as in the  $R_{\nu} = 30$  km sequence of Fernández (2012).

we multiply  $r_{\text{shock}}$  in equation (50) by  $(1 + \Delta r/r_{s0})$  and set  $\Delta r/r_{s0} = 0.3$ . Note however that we are ignoring the effects of convection on this parameterization of the saturated SASI amplitude, basing it instead on results from simulations without neutrino heating. Our analytical treatment also assumes a constant dissociation energy at the shock, which is only an approximate description with the equation of state employed here.

The trend of Figure 10 is evident: shorter periods are obtained with larger neutrino luminosities – which yield larger shock radii – and larger accretion rates. The normalization indicates that massive progenitors with large accretion rates, where strong SASI activity is expected (Müller et al. 2012; Hanke et al. 2013; Ott et al. 2013; Iwakami et al. 2013), can lead to periods  $\sim 100$  ms or less. In contrast, progenitors that have a lower accretion rate and which may be expected to suppress SASI activity (e.g., Müller et al. 2012; Takiwaki et al. 2012; Murphy et al. 2013; Dolence et al. 2013; Couch 2013), would otherwise acquire very moderate amounts of angular momentum if the SASI were present, with minimum periods in the range  $0.3 - 1$  s. Note that the latter value is comparable to the spin periods obtained by Wongwathanarat et al. (2010, 2013).

From an observational point of view, the spin of neutron stars at birth is still poorly constrained. The difficulty comes from the fact that the observed period of pulsars is very different from their initial period because of spin down, and that the true age of most pulsars is unknown. Population synthesis studies nevertheless suggest that a distribution of initial spin peaking around 300 ms is consistent with observations (e.g., Faucher-Giguère & Kaspi 2006). The age of some pulsars can be estimated when they are associated with a supernova remnant, which then allows to constrain their initial spin period. Despite poor statistics and sometimes large uncertainties, these observations suggest that a significant fraction of neutron stars have initial periods longer than 100 ms (e.g. Popov & Turolla 2012 and references therein). The range of pulsar spin periods we obtain is therefore of the same order of magnitude as that inferred from the observations, and we conclude that angular momentum redistribution by a SASI spiral mode can be relevant to explain these observations. Note, however, that rotation initially present in the progenitor, which was neglected in this study, could also add a significant contribution to the angular momentum of the neutron star.

## 6 CONCLUSIONS

We have developed an analytical description of the angular momentum redistribution driven by SASI spiral modes. It is based on a second order perturbative expansion of the flow, which is valid when the amplitude of the spiral mode is small.

Angular momentum redistribution is due to the Reynolds stress of the SASI mode, which can be computed using a linear analysis (§2). For the lowest frequency SASI modes, this Reynolds stress has the same sign as the spherical harmonic index  $m$  of the mode. This causes angular momentum with the same rotation direction as the spiral mode to accumulate below the shock, while angular momentum

with the opposite sign is accreted onto the proto-neutron star.

Higher frequency harmonics have more complex Reynolds stress profiles, showing radial oscillations (Fig. 5). These can be explained by decomposing the velocity perturbations into contributions from the vorticity wave and two acoustic waves propagating up and down (Appendix A). The individual contributions of the vorticity wave and the acoustic wave propagating up create a non-oscillating Reynolds stress profile with the same sign as  $m$ , while the interaction between these two waves causes radial oscillations of the Reynolds stress, with more oscillations being present for the higher frequency harmonics. In a realistic core-collapse supernova context, where multiple modes can be excited by either initial perturbations or convection, a situation with multiple unstable modes is more likely to be obtained.

These analytical results compare favorably with the 3D simulations of Fernández (2010), the Reynolds stress and angular momentum profiles in the linear phase agreeing within 10% for the best resolved simulation, and a few tens of percent at lower resolution.

Although strictly speaking the analytical results are valid only in the linear phase, we have found that they give a reasonable description of the angular momentum density in the non-linear phase if the second term of Equation (24) is omitted to account for the fact that the spiral mode is not growing anymore. As a consequence, nearly all of the SASI active region has the same sign of angular momentum because the matter with opposite angular momentum has already been accreted.

We have also performed a Reynolds decomposition of the numerical models of Fernández (2010) in the saturated phase. The Reynolds stress is again the dominant agent determining the angular momentum profile below the shock. In addition, a contribution from the fluctuating mass flux becomes important near the shock. Both of these effects transport angular momentum outwards, balancing inward transport by advection.

Finally we derived an approximate analytical expression for the angular momentum contained in the SASI spiral wave (eq. 47). This expression depends on the mass accretion rate, the shock and PNS radius, the compression ratio at the shock, and the characteristics of the SASI spiral mode (frequency and amplitude). This allows us to estimate the maximum angular momentum that can be imparted to the neutron star if all the SASI active region is ejected during the explosion. The expected minimum neutron star spin periods in uniform rotation (Fig. 10) are consistent with values estimated by observations of pulsars associated with supernova remnants and by population synthesis studies for the bulk of the pulsar population. Our analysis further suggests that the angular momentum of the nascent neutron star should be positively correlated with the mass accretion rate at the time of explosion if progenitors are slowly rotating. As a consequence, neutron stars born from progenitors with a shallow density profile – for which the SASI should dominate the explosion dynamics (e.g., Müller et al. 2012; Hanke et al. 2013; Iwakami et al. 2013) – should rotate faster on average than those arising from stars with steeper profiles, which are generally less massive.

Obviously, the above prediction is contingent on a very idealised scenario in which the mass cut at explo-

sion coincides with the surface where the angular momentum changes sign. The results of Hanke et al. (2013) indicate that even in progenitors where strong SASI activity is expected, an episodic occurrence of spiral modes can result in no net angular momentum being imparted to the neutron star. Prolonged SASI activity up to the point of explosion, as seen in the 2D models of Müller et al. (2012), is essential for this spin-up mechanism to work. It also requires at least one spiral mode (with spherical harmonics  $\{l, m\}$ ) to dominate over the counterrotating spiral mode (with spherical harmonics  $\{l, -m\}$ ). This may arise naturally from a symmetry breaking that has been observed in some numerical simulations and in the SWASI experiment (Blondin & Mezzacappa 2007; Fernández 2010; Foglizzo et al. 2012), but the timescale and conditions in which this occurs still need to be better understood.

Our analysis applies if the initial rotation of the progenitor is negligibly slow. More generally, the initial spin of neutron stars is likely to result from a combination of angular momentum initially present in the progenitor and that redistributed by the SASI. Given that prograde modes are expected to grow faster (Yamasaki & Foglizzo 2008), the dominance of one such mode would impart angular momentum to the neutron star with a sign opposite to that of the progenitor, in the idealised scenario in which the explosion carries away all the angular momentum of a given sign (Blondin & Mezzacappa 2007). Further studies using a rotating progenitor will be needed to clarify the consequences on the dynamics and on the spin of neutron stars.

We emphasize that the analytical formula for the angular momentum redistributed by a spiral mode depends strongly on the amplitude of the spiral mode. In this study, we did not try to determine analytically the amplitude of the spiral mode, and simply took it as an input from the simulations. A semi-analytical description of the saturation of SASI has been obtained by Guilet et al. (2010). They studied the ability of parasitic instabilities (of Rayleigh-Taylor or Kelvin-Helmholtz type) to grow on a SASI mode and destroy its coherence when it reaches a critical amplitude, thus leading to its saturation. A remaining theoretical uncertainty is the role of shock kinks. Future work addressing the saturation of the SASI can benefit from our theoretical estimate of the maximum angular momentum in the system.

Finally, we note that the present study neglects the effects of magnetic fields, which can transport angular momentum via the Maxwell stress. The influence of a magnetic field on the linear growth of SASI has been studied in a planar toy model by Guilet & Foglizzo (2010). One possible extension of the present study is including magnetic effects in the angular momentum redistribution in spherical or even cylindrical coordinates. Guilet et al. (2011) have shown that Alfvén waves can be amplified in the vicinity of an Alfvén surface, where the advection velocity equals the Alfvén speed. This phenomenon may also have interesting consequences on the angular momentum redistribution.

## ACKNOWLEDGEMENTS

We thank Henrik Latter and Benjamin Favier for helpful discussions and/or comments on the manuscript. We also thank the referee, Thierry Foglizzo, for his insightful report

that helped improve the manuscript. JG acknowledges support from the STFC and the Max-Planck-Princeton Center for Plasma Physics. RF acknowledges support from the University of California Office of the President, and from NSF grants AST-0807444 and AST-1206097.

## APPENDIX A: THE ANGULAR MOMENTUM FLUX DECOMPOSED INTO WAVE CONTRIBUTIONS

The perturbations associated to a SASI mode can be described physically as a superposition of several kinds of waves: two acoustic waves propagating up and down, and an advected wave composed of vorticity and entropy perturbations. In this Appendix we use this decomposition in order to explain the radial profile of the Reynolds stress associated to a SASI mode, in particular the oscillations observed in Section 3.3 in the case of higher frequency harmonics. Strictly speaking, this decomposition requires the use of the WKB approximation and is only valid for the high frequency harmonics of SASI (Foglizzo et al. 2007; Guilet & Foglizzo 2012). In order to get a physical understanding in a cleaner setup, we use a simpler model where the wave decomposition is valid without any approximation: the planar toy model described by Foglizzo (2009). We only give here a brief description of the aspects of the model necessary to understand the present analysis, and the reader is referred to Foglizzo (2009) for a more complete description of the toy model, the equations governing it, and the numerical method used to compute the linear eigenmodes.

In this model a supersonic flow along the  $z$  direction is decelerated through a shock located at  $z = 1$ . The subsonic flow below the shock is uniform until it reaches a localised gravity step located around  $z = 0$  with a width  $H_\nabla$ . The vertical axis  $z$  is analogous to the radial direction in the core collapse, while the transverse  $x$  and  $y$  directions are analogous to the angular directions  $\varphi$  and  $\theta$ . The  $x$  and  $y$  directions are here equivalent and we only consider modes with an  $x$  dependence, which is considered the analog of the azimuthal direction. The linear momentum in the  $x$  direction is then the analog of the angular momentum in spherical geometry. The perturbation of physical variables take the form:

$$\delta A(x, z, t) = \text{Re} \left( \delta \tilde{A}(z) e^{i(k_x x - \omega t)} \right) \quad (\text{A1})$$

A surface integration (analogous to the integration over a spherical surface performed in the rest of the paper) is done on a planar surface at constant  $z$  over the whole horizontal extent of the box. We define a surface average of the Reynolds stress (describing the transport in the  $z$  direction of momentum in the  $x$  direction) as:

$$T_{Rey} \equiv \frac{1}{L_x L_y} \int_0^{L_x} \int_0^{L_y} \rho v_x v_z dx dy \quad (\text{A2})$$

$$T_{Rey} = \frac{\rho_0}{2} \text{Re} \left( \delta \tilde{v}_x \delta \tilde{v}_z^* \right) \quad (\text{A3})$$

Similarly to the angular momentum in the spherical case, the surface averaged linear momentum density in the  $x$  direction is then related to the Reynolds stress by:

$$P_x = -\frac{T_{Rey}}{v_{z0}} + \frac{e^{-2\omega_i \tau_{adv}}}{v_{z0}} \int_{r_{sh}}^r \frac{2\omega_i e^{2\omega_i \tau_{adv}}}{v_{z0}} T_{Rey} dr. \quad (\text{A4})$$

The velocity perturbation of a mode can be decomposed into wave contributions in the following way:

$$\delta v = \delta v^+ + \delta v^- + \delta v^{\text{vort}}, \quad (\text{A5})$$

where the superscripts + and - refer to the acoustic waves propagating down and up respectively, and the superscript vort refers to the shear (or vorticity) wave. Each of the waves has a vertical structure described by a wave vector  $k_z$ , for example for acoustic waves:

$$\delta \tilde{A}^\pm(z) = \delta \tilde{A}_0^\pm e^{ik_z^\pm z}. \quad (\text{A6})$$

The Reynolds stress can then be written as:

$$\begin{aligned} T_{\text{Rey}} = & \frac{\rho_0}{L_x L_y} \int_0^{L_x} \int_0^{L_y} [\delta v_x^+ \delta v_z^+ + \delta v_x^- \delta v_z^- + \delta v_x^{\text{vort}} \delta v_z^{\text{vort}} \\ & + \delta v_x^+ \delta v_z^{\text{vort}} + \delta v_x^{\text{vort}} \delta v_z^+ + \delta v_x^- \delta v_z^{\text{vort}} + \delta v_x^{\text{vort}} \delta v_z^- \\ & + \delta v_x^+ \delta v_z^- + \delta v_x^- \delta v_z^+] d^2 s. \end{aligned} \quad (\text{A7})$$

The first three terms are the individual contributions of the three waves (denoted as  $T_{\text{Rey}}^\pm$  and  $T_{\text{Rey}}^{\text{vort}}$ ). The last six terms are cross terms due to the non linear interaction between the waves. Let us define:

$$T_{\text{Rey}}^{+-} \equiv \frac{\rho_0}{L_x L_y} \int_0^{L_x} \int_0^{L_y} [\delta v_x^+ \delta v_z^- + \delta v_x^- \delta v_z^+] d^2 s \quad (\text{A8})$$

$$T_{\text{Rey}}^{+\text{vort}} \equiv \frac{\rho_0}{L_x L_y} \int_0^{L_x} \int_0^{L_y} [\delta v_x^{\text{vort}} \delta v_z^+ + \delta v_x^+ \delta v_z^{\text{vort}}] d^2 s \quad (\text{A9})$$

$$T_{\text{Rey}}^{-\text{vort}} \equiv \frac{\rho_0}{L_x L_y} \int_0^{L_x} \int_0^{L_y} [\delta v_x^{\text{vort}} \delta v_z^- + \delta v_x^- \delta v_z^{\text{vort}}] d^2 s \quad (\text{A10})$$

These cross terms do not generally vanish (although some may in certain cases) and depend on the relative phase between the different waves. The total Reynolds stress is then written as the sum of six terms:

$$T_{\text{Rey}} = T_{\text{Rey}}^+ + T_{\text{Rey}}^- + T_{\text{Rey}}^{\text{vort}} + T_{\text{Rey}}^{+-} + T_{\text{Rey}}^{-\text{vort}} + T_{\text{Rey}}^{+\text{vort}} \quad (\text{A11})$$

Next we assess the relative importance of these different contributions, as well as their sign and vertical profile. We start by general considerations on each of these contributions separately (Sections A1 and A2) and then describe the wave decomposition below the perturbed shock and the resulting vertical profile of Reynolds stress between the shock and the coupling region (Section A3).

## A1 Acoustic waves

Consider a planar acoustic wave with a wave vector  $\mathbf{k} = k_x \mathbf{u}_x + k_z \mathbf{u}_z$  and velocity amplitude  $\delta \tilde{v}$ . Its velocity perturbation is given by:

$$\delta \mathbf{v} = \delta \tilde{v} \frac{\mathbf{k}}{k} \quad (\text{A12})$$

The Reynolds stress is then (assuming  $k_z$  is a real number):

$$T_{\text{Rey}}^{\text{ac}} = \frac{\rho_0}{2} |\delta \tilde{v}|^2 \frac{k_x k_z}{k^2} \quad (\text{A13})$$

This means that an acoustic wave propagating up ( $k_z > 0$ ) creates an upwards flux of momentum oriented with the same sign as  $k_x$ , while a wave propagating down ( $k_z < 0$ ) creates a flux with the opposite sign. The intensity of this flux is maximum when  $k_x = k_z$ , i.e. when the wave propagates in an oblique direction with an angle of  $45^\circ$  with the

vertical. The reason is that large velocities in both horizontal and vertical directions are needed to transport momentum efficiently.

In the presence of advection, the vertical wave number can be expressed as a function of the frequency  $\omega$  and the horizontal wave number as:

$$k_z^\pm = \frac{\omega}{c} \frac{\mathcal{M} \mp \mu}{1 - \mathcal{M}^2}, \quad (\text{A14})$$

where  $\mu$  is defined by  $\mu^2 = 1 - k_x^2 c^2 (1 - \mathcal{M}^2) / \omega^2$ . Assuming that  $\omega$  and  $\mu$  are real (i.e. the wave is not evanescent), the Reynolds stress associated to an individual wave (+ or -) is then:

$$T_{\text{Rey}}^\pm = \frac{\rho_0}{2} |\delta \tilde{v}|^2 \frac{\omega k_x c (\mathcal{M} \mp \mu) (1 - \mathcal{M}^2)}{k_x^2 c^2 (1 - \mathcal{M}^2)^2 + \omega^2 (\mathcal{M} \mp \mu)^2}. \quad (\text{A15})$$

The cross term coming from the interaction between the two acoustic waves + and - can be written:

$$T_{\text{Rey}}^{+-} = \frac{\rho_0}{2} \text{Re} \left( \delta \tilde{v}^+ \delta \tilde{v}^{-*} \right) \frac{k_x (k_z^+ + k_z^-)}{k^+ k^-}, \quad (\text{A16})$$

where  $k^\pm = \sqrt{k_x^2 + k_z^{\pm 2}}$ . In the absence of advection ( $\mathcal{M} = 0$ ), then  $k_z^+ = -k_z^-$  (for a wave of a given frequency) and  $T^{+-} = 0$ : the two terms in Equation (A8) cancel each other. In this special case, the Reynolds stress of the two superposed acoustic waves is the sum of the individual contributions. In the presence of advection however, the cross term does not vanish but may be expected to be small for small Mach numbers:

$$T_{\text{Rey}}^{+-} = \rho_0 \text{Re} \left( \delta \tilde{v}^+ \delta \tilde{v}^{-*} \right) \frac{k_x}{k^+ k^-} \frac{\omega}{c} \frac{\mathcal{M}}{1 - \mathcal{M}^2}. \quad (\text{A17})$$

Note that the term  $\text{Re} \left( \delta \tilde{v}^+ \delta \tilde{v}^{-*} \right)$  has the following vertical structure:

$$\text{Re} \left( \delta \tilde{v}^+ \delta \tilde{v}^{-*} \right) = \text{Re} \left( \delta \tilde{v}_0^+ \delta \tilde{v}_0^{-*} e^{i(k_z^+ - k_z^-)z} \right), \quad (\text{A18})$$

i.e. it oscillates with a wave number  $k_z^\pm = k_z^+ - k_z^-$ . Contrary to the Reynolds stress contribution of an individual wave which does not depend on its phase and therefore does not oscillate, the cross term depends on the relative phase of the two waves and therefore displays vertical oscillations with a wave vector that is the difference between the wave vectors of the two waves.

## A2 Shear wave

A shear wave with a wave vector  $\mathbf{k} = k_x \mathbf{u}_x + k_z \mathbf{u}_z$  (with  $k_z = \omega/v_0 < 0$ ) and velocity amplitude  $\delta \tilde{v}$  has the following velocity vector:

$$\delta \mathbf{v} = \delta \tilde{v} \mathbf{u}_y \times \frac{\mathbf{k}}{k}. \quad (\text{A19})$$

The Reynolds stress of this wave is then:

$$T_{\text{Rey}}^{\text{vort}} = -\frac{\rho_0}{2} |\delta \tilde{v}|^2 \frac{k_x k_z}{k^2} \quad (\text{A20})$$

$$= -\frac{\rho_0}{2} |\delta \tilde{v}|^2 \frac{1}{\frac{\omega}{k_x v} + \frac{k_x v}{\omega}}. \quad (\text{A21})$$

Note that this corresponds to a momentum flux opposite to that of an acoustic wave with the same wave vector and velocity amplitude (compare Equations (A13) and (A20)). The reason is that the velocity associated with an acoustic wave is parallel to its wave vector, while the velocity of

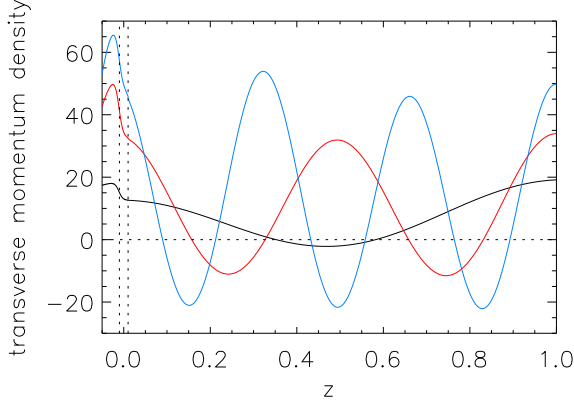


**Figure A1.** Vertical profile of the transverse momentum in the planar toy model of Foglizzo (2009) with the parameters  $L_x = 4$ ,  $n_x = 1$ ,  $c_{\text{in}}^2/c_{\text{out}}^2 = 0.75$ ,  $H_{\nabla} = 0.02H$ , and a strong shock ( $\mathcal{M}_1 \rightarrow \infty$ ). The fundamental mode is shown with a black line, the first higher frequency harmonic with a red line, and the second harmonic with a blue line.

a shear wave is perpendicular to its wave vector (because  $\nabla \cdot \mathbf{v} = i\mathbf{k} \cdot \mathbf{v} = 0$ ). As  $k_z$  is negative, the Reynolds stress carried by the shear wave has the same sign as  $k_x$ . For a given velocity amplitude, the optimum orientation of the wave vector is again  $45^\circ$  with respect to the vertical.

The cross term between the vorticity wave and the acoustic waves can be written as:

$$T_{\text{Rey}}^{\pm \text{vort}} = \frac{\rho_0}{2} \text{Re} (\delta \tilde{v}^{\text{vort}} \delta \tilde{v}^{\pm *}) \frac{k_z^{\text{vort}} k_z^{\pm} - k_x^2}{k_{\pm}^2 k^{\text{vort}}}, \quad (\text{A22})$$

which oscillates in the vertical direction with a wave number  $k_z^{\text{vort}\pm} = k_z^{\text{vort}} - k_z^{\pm}$ .

### A3 Vertical profile of the Reynolds stress

The vertical profiles of transverse momentum induced by three modes with a transverse structure  $n_x = 1$  are shown in Figure A1: the fundamental mode (black line), the first higher frequency harmonics (red line) and the second higher frequency harmonics (blue line). They show oscillations that are very similar to the radial oscillations observed in the spherical model in Section 3.3. The fundamental mode makes one oscillation, the first harmonics two oscillations and the third harmonics three oscillations between the shock and the potential jump. To understand this feature, we show in Figure A2 the decomposition of the Reynolds stress into the six contributions coming from the three types of waves and the interaction between them. There are three significant contributions: the vorticity wave (red full line), the acoustic wave propagating up (blue full line) and the interaction between these two waves (red dashed line). The other three contributions are significantly smaller: the acoustic wave propagating down and its interaction with the two other waves. This is consistent with the fact that SASI is caused by an advective-acoustic cycle in which the advected vorticity wave and the acoustic wave propagating up play a dominant role, while the acoustic wave propagating down plays only a minor role. The individual contributions of the vorticity and acoustic waves do not oscillate and are both

positive (for  $k_x > 0$ ) as shown in the last two subsections. The oscillations in the Reynolds stress profile are due to the interaction between the vorticity wave and the acoustic wave propagating up. As shown in the previous section, the Reynolds stress resulting from this interaction  $T_{\text{Rey}}^{\text{vort}}$  oscillates with a wave vector  $:\omega/v - k_z^-$ . If there is no phase shift at the couplings (at the shock and in the gradient), then the phase relation determining the frequency of advective-acoustic modes is  $:(\omega/v - k_z^-)H = 2n_z\pi$  (this is equivalent to Equation 34 of Guilet & Foglizzo (2012)), where  $H$  is the distance between the shock and the potential jump and  $n_z$  is an integer number defining the mode considered ( $n_z = 1$  for the fundamental mode,  $n_z = 2$  for the first harmonics,  $n_z = 3$  for the second harmonics). This therefore explains the number of oscillations observed in the Reynolds stress profile.

The relative importance of the different contributions can be determined analytically by using the boundary conditions at the shock. For simplicity we restrict our analysis to the case of a strong shock and an eigenfrequency  $\omega$  which is real and such that acoustic waves are not evanescent (i.e.  $\mu^2 > 0$ ). Neglecting the growth rate leads to an error which is less than 1% of the total Reynolds stress. The velocity perturbations below the shock and the resulting Reynolds stress can be written as :

$$\delta v_{x\text{sh}} = \frac{2}{\gamma - 1} i k_x v_{\text{sh}} \Delta z \quad (\text{A23})$$

$$\delta v_{z\text{sh}} = -\frac{2}{\gamma + 1} i \omega \Delta z \quad (\text{A24})$$

$$T_{\text{Rey}} = -\frac{2}{\gamma^2 - 1} \rho_0 v_{\text{sh}} k_x \omega \Delta z^2 \quad (\text{A25})$$

The  $y$ -component of the vorticity created by the shock oscillations is (Foglizzo 2009):

$$\delta w_{\text{sh}} = -\frac{4}{\gamma^2 - 1} \omega k_x \Delta z, \quad (\text{A26})$$

and the contribution of the shear wave to the Reynolds stress at the shock is then:

$$T_{\text{Rey}}^{\text{vort}} = \frac{4}{\gamma^2 - 1} \frac{1}{\left(\frac{\omega}{k_x v} + \frac{k_x v}{\omega}\right)^2} T_{\text{Rey}}. \quad (\text{A27})$$

The fraction of the total Reynolds stress contributed by the vorticity wave is maximum if  $\frac{\omega}{k_x v} = 1$ , i.e. if the vorticity is inclined by an angle of  $45^\circ$  with respect to the vertical (recall that  $k_z = \omega/v$ ). When  $\frac{\omega}{k_x v}$  goes to zero or infinity this fraction goes to zero. For the fundamental mode and the parameters used in Figures A1 and A2,  $\omega/(k_x v) \simeq 3$  and  $T^{\text{vort}} \simeq 0.5 T_{\text{Rey}}$ . In the case of higher frequency harmonics the vorticity wave contributes less to the total Reynolds stress in agreement with Figure A2. This comes from the fact that, when the frequency increases, the vertical component of the wave vector of the shear wave becomes more and more dominant. Since the velocity perturbation associated to a shear wave is perpendicular to its wave vector, the velocity is then mostly horizontal. As a result the vertical component of the velocity associated to the shear wave decreases, thus decreasing the associated Reynolds stress.

In order to extrapolate this result to the spherical model, one can estimate the equivalent of the parameter  $\omega/(k_x v)$  to be  $\omega r_{\text{sh}} / (\sqrt{l(l+1)} v_{\text{sh}})$ . For the fundamental mode when  $r_* = 0.5 r_{\text{sh}}$ , this parameter is approximately 3.5,

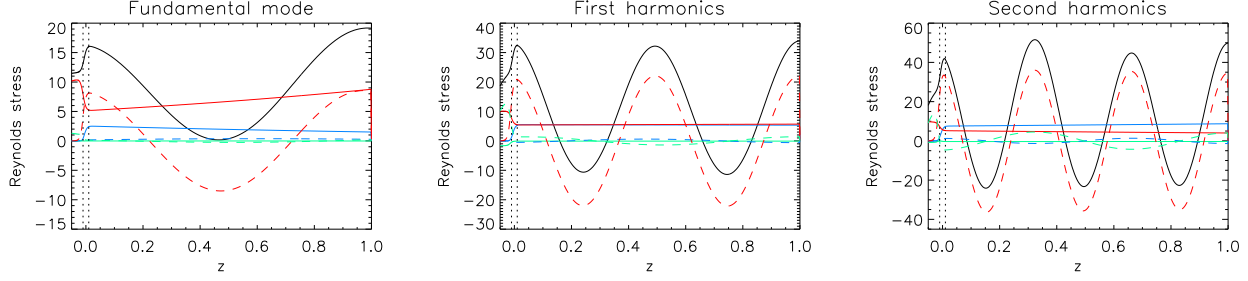


**Figure A2.** Decomposition of the Reynolds stress into wave contributions in the planar toy model of Foglizzo (2009). The parameters are the same as those used in Figure A1. The different lines show the total Reynolds stress  $T_{\text{Rey}}$  (black line), the contributions of individual waves : the vorticity wave  $T_{\text{Rey}}^{\text{vort}}$  (red full line), the acoustic wave propagating up  $T_{\text{Rey}}^-$  (blue full line), and the acoustic wave propagating down  $T_{\text{Rey}}^+$  (green full line), and finally the contributions due to the interaction between two types of waves : the vorticity wave and the acoustic wave propagating up  $T_{\text{Rey}}^{\text{vort}-}$  (red dashed line), the vorticity wave and the acoustic wave propagating down  $T_{\text{Rey}}^{\text{vort}+}$  (green dashed line), and the two acoustic waves  $T_{\text{Rey}}^{+-}$  (blue dashed line). The three panels show three different modes with increasing frequencies : fundamental mode (left panel), first higher frequency harmonics (middle panel), and second higher frequency harmonics (right panel). The vertical dotted lines show the extent of the potential jump.

therefore rather close to its value for the fundamental mode of the planar toy model. We therefore expect that the vorticity wave contributes to about half of the total Reynolds stress. This feature can be expected to hold generally for the most unstable mode. Indeed the most unstable mode corresponds to acoustic waves being close to horizontal propagation (see Figure 8 and 10 of Guilet & Foglizzo (2012)), i.e.  $\omega \simeq kc_s$  where  $k$  is the transverse wave number and  $c_s$  is the sound speed. Therefore the most unstable mode should satisfy  $\omega/(kv) \simeq 1/M_{\text{sh}} \simeq 3$ .

The pressure perturbation below the shock can be expressed as:

$$\left(\frac{\delta P}{\gamma P}\right)_{\text{sh}} = \frac{2\gamma - 1}{\gamma\gamma + 1} \frac{i\omega\Delta z}{v_{\text{sh}}}. \quad (\text{A28})$$

This can be decomposed into the two acoustic waves propagating up and down, which have the following pressure and velocity perturbations:

$$\left(\frac{\delta P^\pm}{\gamma P}\right)_{\text{sh}} = \frac{\gamma - 1}{\gamma(\gamma + 1)} \frac{i\omega\Delta z}{v_{\text{sh}}} \left(1 \mp \frac{\mu}{2\mathcal{M}}\right), \quad (\text{A29})$$

$$\delta v_{\text{sh}}^\pm = -\frac{1}{\gamma + 1} \sqrt{\frac{2(\gamma - 1)}{\gamma}} i\omega\Delta z \left(1 \mp \frac{\mu}{2\mathcal{M}}\right). \quad (\text{A30})$$

The Reynolds stress associated to each of these two acoustic waves can then be obtained by substituting this velocity perturbation into Equation (A15). Note that the velocity amplitude of the acoustic wave propagating up (noted -) is always larger than that of the acoustic wave propagating down (noted +): the acoustic wave is damped at the reflection at the shock as was already shown by Foglizzo (2009). This explains why the three terms involving the acoustic wave propagating down ( $T_{\text{Rey}}^+$ ,  $T_{\text{Rey}}^{\text{vort}+}$ , and  $T_{\text{Rey}}^{+-}$ ) play only a very minor role in the Reynolds stress.

The Reynolds stress from the interaction between the vorticity wave and the acoustic waves can be found using Equation (A22) and the velocity perturbations of the waves:

$$T_{\text{Rey}}^{\pm\text{vort}} = \frac{1}{\gamma + 1} \sqrt{\frac{2(\gamma - 1)}{\gamma}} \frac{\omega}{v} \frac{\left(1 \mp \frac{\mu}{2\mathcal{M}}\right) \left(\frac{\omega^2}{v^2} \frac{\mathcal{M} \mp \mu}{1 - \mathcal{M}^2} - k_x^2\right)}{\left(\frac{\omega^2}{v^2} + k_x^2\right) \sqrt{\frac{\omega^2}{c^2} \left(\frac{\mathcal{M} \mp \mu}{1 - \mathcal{M}^2}\right)^2 + k_x^2}} T_{\text{Rey}}$$

(A31)

The contribution from the interaction between the vorticity wave and the acoustic wave propagating up has the same sign as the total Reynolds stress and contributes a significant fraction of it: about half for the fundamental mode, and more than two thirds for the second harmonics. The fact that it contributes a large fraction of the total stress at high frequency can be understood qualitatively as follows. At high frequency, the wave vectors of both the vorticity wave and the acoustic wave are mostly vertical. As a result, the velocity perturbation of the vorticity wave is mostly horizontal while the velocity perturbation of the acoustic wave is mostly vertical. Neither of the waves independently transports efficiently angular momentum because this needs both horizontal and vertical velocities. But the interaction of the two waves is very efficient at transporting angular momentum by combining the horizontal velocity of the vorticity wave and the vertical velocity of the acoustic wave.

## APPENDIX B: MEASURE OF THE SPIRAL MODES AMPLITUDE IN THE LINEAR PHASE

In this appendix we describe the method we used in Section 3 in order to compute the amplitude of the two spiral modes  $\pm m$  in the linear phase of SASI. We describe successively two different methods based on a fit of the time-evolution either of the displacement amplitude of the shock (Section B1) or of the transverse velocities in the postshock flow (Section B2). The results of these two methods are then compared in Section B3.

### B1 Method using the shock displacement

To be specific, we here focus on the case of spiral modes with  $m = \pm 1$  (Section 3.1 and 3.3) but the same method can be applied to the case of  $m = \pm 2$  as well (Section 3.2). The amplitude of the shock deformation has been projected onto real spherical harmonics along the x and y axis (we assume



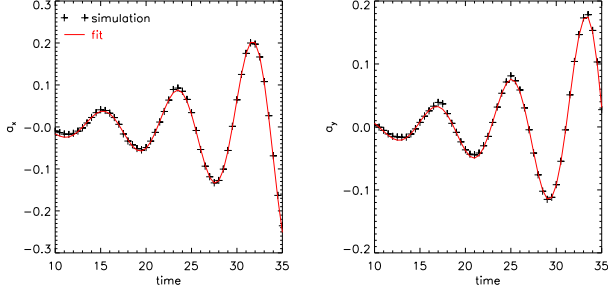


**Figure B1.** Fit of the amplitude of the shock deformation projected onto spherical harmonics in the linear phase of SASI. Left panel: along the x axis. Right panel: along the y axis. The simulation results are shown with black + signs, while the fit is shown with red line.

that the component on the z axis is negligible) defined as:

$$Y_{1x} = \sqrt{\frac{3}{4\pi}} \sin \theta \cos \phi \quad (\text{B1})$$

$$Y_{1y} = \sqrt{\frac{3}{4\pi}} \sin \theta \sin \phi \quad (\text{B2})$$

(Note that  $Y_{1x}$  was noted  $Y_1^1$  in Fernández (2010), while  $Y_{1y}$  was noted  $Y_1^{-1}$ .) The time evolution of these spherical harmonics amplitudes is then fitted using a function of the form:

$$f(t) = A \cos(\omega_r t + \Phi) \exp \omega_i t, \quad (\text{B3})$$

which has four parameters: the amplitude  $A$ , the phase  $\Phi$ , the frequency  $\omega_r$  and the growth rate  $\omega_i$ . These are measured for both axis x and y (Figure B1). As expected, the frequency and growth rate are the same on both axis within small numerical errors, and we later use the average of the two values.

These two sloshing modes can be equivalently described as two counter-rotating spiral modes, which are described using complex spherical harmonics defined as:

$$Y_1^1 = -\sqrt{\frac{3}{8\pi}} \sin \theta e^{i\phi} \quad (\text{B4})$$

$$Y_1^{-1} = \sqrt{\frac{3}{8\pi}} \sin \theta e^{-i\phi} \quad (\text{B5})$$

The sloshing mode along the  $x$  axis ( $\phi = 0$ ) with amplitude  $A_x$  and phase  $\Phi_x$  can be decomposed into two spiral modes of equal amplitude but different phase as:

$$A_x \cos(\omega_r t + \Phi_x) e^{\omega_i t} Y_{1x} = \text{Re} \left[ \frac{A_x}{\sqrt{2}} e^{-i\phi_x} e^{-i\omega t} (-Y_1^1 + Y_1^{-1}) \right] \quad (\text{B6})$$

Similarly the sloshing mode along the  $y$ -axis can be decomposed into two spiral modes of equal amplitude and phase:

$$A_y \cos(\omega_r t + \Phi_y) e^{\omega_i t} Y_{1y} = \text{Re} \left[ \frac{A_y}{\sqrt{2}} e^{-i(\phi_y - \pi/2)} e^{-i\omega t} (Y_1^1 + Y_1^{-1}) \right] \quad (\text{B7})$$

Combining these two expressions, we finally obtain the

amplitude and phase of the two spiral modes  $m = \pm 1$  as:

$$A_1 e^{-i\phi_1} = -\frac{A_x}{\sqrt{2}} e^{-i\phi_x} + \frac{A_y}{\sqrt{2}} e^{-i(\phi_y - \pi/2)} \quad (\text{B8})$$

$$A_{-1} e^{-i\phi_{-1}} = \frac{A_x}{\sqrt{2}} e^{-i\phi_x} + \frac{A_y}{\sqrt{2}} e^{-i(\phi_y - \pi/2)} \quad (\text{B9})$$

Note that here the amplitude of the sloshing mode is expressed in terms of real spherical harmonics, while that of the spiral modes is expressed in terms of complex spherical harmonics which have a different normalisation (by a factor  $1/\sqrt{2}$ ).

## B2 Method using transverse velocities

To check our results, we have computed the amplitude of spiral modes with an alternative method involving the transverse velocities of the flow. To this end we make use of the quantity  $\delta A$  defined in Foglizzo et al. (2007):

$$\delta A \equiv \frac{r}{\sin \theta} \left[ \frac{\partial}{\partial \theta} (\sin \theta \delta v_\theta) + \frac{\partial}{\partial \phi} \delta v_\phi \right] \quad (\text{B10})$$

$$= \frac{1}{i\omega} [\delta K - \ell(\ell+1)f], \quad (\text{B11})$$

which vanishes for a spherically symmetric flow, and which has been previously used to compute the perturbation amplitude by Scheck et al. (2008).

The transverse velocities have the dependence of a vector spherical harmonic,

$$\delta \mathbf{v}_\perp = \delta v_\theta \hat{\theta} + \delta v_\phi \hat{\phi} = \delta \tilde{v}_\perp e^{-i\omega t} \Psi_{\ell m}(\theta, \phi), \quad (\text{B12})$$

with

$$\Psi_{\ell m} = r \nabla Y_\ell^m = \hat{\theta} \frac{\partial}{\partial \theta} Y_\ell^m + \hat{\phi} \frac{1}{\sin \theta} \frac{\partial}{\partial \phi} Y_\ell^m, \quad (\text{B13})$$

where  $\hat{\theta}$  and  $\hat{\phi}$  are the unit coordinate vectors in the polar and azimuthal directions, respectively. Equation (B10) thus implies that  $\delta A$  is proportional to a scalar spherical harmonic  $Y_\ell^m$ , with amplitude

$$\delta \tilde{A} = -\ell(\ell+1)r \delta \tilde{v}_\perp, \quad (\text{B14})$$

and also proportional to the shock displacement amplitude  $\Delta \tilde{r}$ .

To find  $\Delta \tilde{r}$  from the simulation, we first project the transverse velocity field into the appropriate vector spherical harmonic to obtain a coefficient

$$\tilde{v}_\perp, \text{ sim}(r, t) = \frac{1}{\ell(\ell+1)} \int \mathbf{v}_\perp(r, \theta, \phi, t) \cdot \Psi_{\ell m}^* d\Omega. \quad (\text{B15})$$

$\Psi_{\ell m}$  is computed from real spherical harmonics along  $x$  and  $y$  axis, and the velocity coefficient is therefore real. The time evolution of these velocity amplitudes at a chosen radius is then fitted using the same method as in last subsection. The complex amplitude of spiral modes thus obtained  $\Delta \tilde{v}$  is then converted into a complex shock displacement amplitude by using equation (B14) in the following way

$$\Delta \tilde{r} = \frac{-\ell(\ell+1)r \Delta \tilde{v}}{\delta \tilde{A}}, \quad (\text{B16})$$

where the complex amplitude  $\delta \tilde{A}$  is obtained from the linear stability analysis with a unit shock displacement at phase zero.

**B3 Comparison of the two methods**

We have applied the two above methods to the linear growth phase of model R5\_L11\_HR (analysed in Section 3.1). The eigenfrequencies obtained from the fit match the linear analysis to within 0.5% for the oscillation frequency and to within 5% for the growth rate. The first method gives the following amplitudes of the two spiral modes  $m = 1$  and  $m = -1$  at time  $t = 30$ :  $A_1 = 0.206$  and  $A_{-1} = 0.051$ . This can be compared to the amplitude measured using transverse velocities at radius  $r_1 = 0.6$ :  $A_1 = 0.232$  and  $A_{-1} = 0.052$ , and at radius  $r_2 = 0.8$ :  $A_1 = 0.229$  and  $A_{-1} = 0.055$ . The two measures using the second method at different radii are in good agreement with each other, while they are  $\sim 10\%$  larger than the result of the first method. In Section 3, we have chosen to use the result of the second method because it provides a better match to the radial profiles of linear perturbations.

For model R6\_L22\_P2 (analysed in Section 3.2), the first method gives:  $A_2 = 0.180$  and  $A_{-2} = 0.022$ . The second method using  $r_1 = 0.7$  gives:  $A_2 = 0.177$  and  $A_{-2} = 0.017$ , while using  $r_2 = 0.8$  we obtain:  $A_2 = 0.185$  and  $A_{-2} = 0.021$ . The agreement between the two methods is here better than for model R5\_L11\_HR in spite of the lower resolution.

**REFERENCES**

- Bethe H. A., Wilson J. R., 1985, *ApJ*, 295, 14  
 Blondin J. M., Mezzacappa A., 2007, *Nature*, 445, 58  
 Blondin J. M., Mezzacappa A., DeMarino C., 2003, *ApJ*, 584, 971  
 Blondin J. M., Shaw S., 2007, *ApJ*, 656, 366  
 Burrows A., 2013, *RMP*, 85, 245  
 Burrows A., Dolence J. C., Murphy J. W., 2012, *ApJ*, 759, 5  
 Couch S. M., 2013, *ApJ*, 775, 35  
 Dolence J. C., Burrows A., Murphy J. W., Nordhaus J., 2013, *ApJ*, 765, 110  
 Faucher-Giguère C.-A., Kaspi V. M., 2006, *ApJ*, 643, 332  
 Fernández R., 2010, *ApJ*, 725, 1563  
 Fernández R., 2012, *ApJ*, 749, 142  
 Fernández R., Müller B., Foglizzo T., Janka H.-T., 2014, *MNRAS*, 440, 2763  
 Fernández R., Thompson C., 2009a, *ApJ*, 703, 1464  
 Fernández R., Thompson C., 2009b, *ApJ*, 697, 1827  
 Foglizzo T., 2009, *ApJ*, 694, 820  
 Foglizzo T., Galletti P., Scheck L., Janka H.-T., 2007, *ApJ*, 654, 1006  
 Foglizzo T., Masset F., Guilet J., Durand G., 2012, *PRL*, 108, 051103  
 Foglizzo T., Scheck L., Janka H.-T., 2006, *ApJ*, 652, 1436  
 Guilet J., Foglizzo T., 2010, *ApJ*, 711, 99  
 Guilet J., Foglizzo T., 2012, *MNRAS*, 421, 546  
 Guilet J., Foglizzo T., Fromang S., 2011, *ApJ*, 729, 71  
 Guilet J., Sato J., Foglizzo T., 2010, *ApJ*, 713, 1350  
 Hanke F., Müller B., Wongwathanarat A., Marek A., Janka H.-T., 2013, *ApJ*, 770, 66  
 Herant M., Benz W., Colgate S., 1992, *ApJ*, 395, 642  
 Iwakami W., Kotake K., Ohnishi N., Yamada S., Sawada K., 2008, *ApJ*, 678, 1207  
 Iwakami W., Kotake K., Ohnishi N., Yamada S., Sawada K., 2009, *ApJ*, 700, 232  
 Iwakami W., Nagakura H., Yamada S., 2013, *ApJ*, submitted, arXiv:1308.0829  
 Janka H.-T., 2012, *Ann. Rev. Nuc. Part. Sci.*, 62, 407  
 Janka H.-T., Hanke F., Hüdepohl L., Marek A., Müller B., Obergaulinger M., 2012, *Prog. Th. Ex. Phys.*, 2012, 010000  
 Janka H.-T., Keil W., 1998, in L. Labhardt, B. Binggeli, & R. Buser ed., *Supernovae and cosmology Perspectives of Core-Collapse Supernovae beyond SN 1987A*. p. 7  
 Liebendörfer M., Mezzacappa A., Thielemann F.-K., Messer O. E., Hix W. R., Bruenn S. W., 2001, *Phys. Rev. D*, 63, 103004  
 Marek A., Janka H.-T., 2009, *ApJ*, 694, 664  
 Müller B., Janka H.-T., Heger A., 2012, *ApJ*, 761, 72  
 Murphy J. W., Burrows A., 2008, *ApJ*, 688, 1159  
 Murphy J. W., Dolence J. C., Burrows A., 2013, *ApJ*, 771, 52  
 Murphy J. W., Meakin C., 2011, *ApJ*, 742, 74  
 O'Connor E., Ott C. D., 2010, *Classical and Quantum Gravity*, 27, 114103  
 Ott C. D., Abdikamalov E., Mösta P., Haas R., Drasco S., O'Connor E. P., Reisswig C., Meakin C. A., Schnetter E., 2013, *ApJ*, 768, 115  
 Popov S. B., Turolla R., 2012, *Ap&SS*, 341, 457  
 Rampp M., Janka H.-T., 2002, *A&A*, 396, 361  
 Rantsiou E., Burrows A., Nordhaus J., Almgren A., 2011, *ApJ*, 732, 57  
 Sato J., Foglizzo T., Fromang S., 2009, *ApJ*, 694, 833  
 Scheck L., Janka H.-T., Foglizzo T., Kifonidis K., 2008, *A&A*, 477, 931  
 Shen H., Toki H., Oyamatsu K., Sumiyoshi K., 1998, *Nuclear Physics A*, 637, 435  
 Sumiyoshi K., Yamada S., Suzuki H., Shen H., Chiba S., Toki H., 2005, *ApJ*, 629, 922  
 Takiwaki T., Kotake K., Suwa Y., 2012, *ApJ*, 749, 98  
 Thompson C., 2000, *ApJ*, 534, 915  
 Thompson T. A., Burrows A., Pinto P. A., 2003, *ApJ*, 592, 434  
 Thompson T. A., Quataert E., Burrows A., 2005, *ApJ*, 620, 861  
 Wongwathanarat A., Janka H.-T., Müller E., 2010, *ApJL*, 725, L106  
 Wongwathanarat A., Janka H.-T., Müller E., 2013, *A&A*, 552, A126  
 Yamasaki T., Foglizzo T., 2008, *ApJ*, 679, 607  
 Yamasaki T., Yamada S., 2007, *ApJ*, 656, 1019

This paper has been typeset from a  $\text{\TeX}/\text{\LaTeX}$  file prepared by the author.